DIRECT NUMERICAL SIMULATION ANALYSIS OF HIGH-SPEED COMPRESSIBLE TURBULENT REACTING FLOWS AT PROPULSION-RELEVANT CONDITIONS

A Thesis

By

LAURA ROSE O'NEILL

Submitted to the Office of Graduate and Professional Studies of
Texas A&M University
in partial fulfillment of the requirements for the degree of

MASTER OF SCIENCE

Chair of Committee,	Alexei Poludnenko
Committee Members,	Adonios Karpetis
	Waruna Kulatilaka
Head of Department,	Rodney Bowersox

August 2019

Major Subject: Aerospace Engineering

ABSTRACT

A direct numerical simulation (DNS) of a propagating H_2-air flame in a semi-confined geometry is performed and analyzed. Simulation setup imitates the flow conditions in the Turbulent Shock Tube (TST) facility developed by the University of Central Florida. This facility and numerical configuration are designed for the study of high-speed, highly compressible premixed turbulent flames over a broad range of conditions including extreme ones leading to the deflagration-to-detonation transition (DDT). Present DNS is performed using the code Athena-RFX with a simplified single-step Arrhenius kinetics model representing a stoichiometric H_2-air mixture. The combustion regimes that are accessed using this realistic configuration are at simultaneously high turbulent length and velocity scales, which push the extreme boundaries previously studied regimes. Analysis of the overall flame dynamics shows that the displacement-based turbulent flame speed does not represent the turbulent burning velocity with sufficient accuracy at these extreme regimes. Turbulent flow speed and enstrophy analysis suggest strong turbulence amplification by the flame, in agreement with the results of prior DNS performed in a more idealized setting of a flame interacting with an externally driven homogeneous, isotropic turbulence. Ultimately, this thesis develops a complementary numerical and experimental platform for the fundamental studies of high-speed, highly compressible turbulent combustion regimes directly relevant to novel aerospace propulsion applications, such as scramjets and detonation-based engines.

CONTRIBUTORS AND FUNDING SOURCES

Contributors

This work was supervised by a thesis committee consisting of my advisor Professor Alexei Poludnenko, Professor Adonios Karpetis of the Department of Aerospace Engineering, and Professor Waruna Kulatilaka of the Department of Mechanical Engineering.

Direct numerical simulations (DNS) were produced jointly between myself and my chair, Dr. Alexei Poludnenko. Experimental procedures and analysis were completed by Dr. Kareem Ahmed and Jessica Chambers of the Propulsion and Energy Research Lab at the University of Central Florida. Lagrangian analysis of multi-step chemical DNS in Appendix B was performed by Sai Sandeep Dammati. All other work conducted for the thesis was completed by the student independently.

Funding Sources

This work was supported in part by the Texas A&M University and the Texas A&M Engineering Experiment Station funding provided to Professor Poludnenko. Computing resources were provided by the Department of Defense High Performance Computing Modernization Program under a Frontier project award, and by the Naval Research Laboratory.

TABLE OF CONTENTS

Page

LIST OF FIGURES

Page

LIST OF TABLES

Page

CHAPTER I

INTRODUCTION

Turbulent reacting flows are involved in the operation of most combustion systems of practical importance. Historically, experimental testing has been the primary driver of advances in the development of propulsion systems, e.g. in aircraft and rocket engines. As more advanced propulsion systems are developed, the "trial-and-error" method has become too costly to rely on alone. Numerical simulations provide both cost savings as well as a tool to gain deeper insight into the fundamental nature of turbulent flames within combustors, especially in leaner mixtures, at higher pressures, speeds, levels of premixedness, and at off-design conditions, which can drive further developments [1].

Toward this cost-minded aim, modeling approaches are highly advantageous, although they face a practical problem due to the nature of realistic propulsion system applications. While characteristic combustor scales can be of the order of centimeters, laminar flame thickness may lie on the sub-millimeter scale, and turbulent scales may be mere micrometers. Ideally, this entire range of scales would be fully resolved, but such a wide scope surpasses the current capabilities of modern high-performance computing (HPC) systems.

One common option when faced with this so-called "tyranny of scales" is Large-Eddy Simulation (LES), which resolves the larger, dynamically important scales and models the complexities generated by turbulence and combustion on the small scales [2-5]. While LES has been successful in using simplified subgrid-scale models to obtain accurate overall results in many applications [6], this approach is inherently limited by the validity of its models.

Reacting flow fields in propulsion systems, such as those within a scramjet combustor, are high speed, strongly compressible, and highly turbulent. These criteria put the fluid dynamics of

interest beyond the comfortable range of LES. Therefore, in these conditions, Direct Numerical Simulation (DNS) is still required to advance the fundamental understanding of turbulent reacting flow physics.

With these considerations, other methods must be employed to reduce or simplify the large, complex domain of a combustor to within the range of DNS. Three elements contribute to this dilemma: the extreme regimes which drive down turbulence and time scales, the large size of realistic industrial or experimental facilities, and the myriad of chemical species and mechanisms in real fuels. Here, it is worth noting the distinction between industrial and experimental facilities. Experimental facilities are "artificial" facilities designed to generate conditions of interest, e.g. a shock tube. On the other side of the spectrum, industrial facilities are those which are directly used in applications, e.g. a combustor. Simulations may aim to represent either sort of facility, something in-between, or neither, as in the case of "flame in the box" DNS.

Development and advancement of novel aerospace propulsion applications, such as scramjets and detonation-based engines, poses the need for investigation into the extreme regimes under which they operate. To maintain relevance to these applications, extreme regimes under realistic physical domain conditions must be explored.

Previous work has studied configurations such as the DLR-type PRECCINSTA burner [2, 3, 7, 8]. This setup represents a lab-based industrial facility which can be closely applied to industrial jet engines. Additional work concerning this configuration is detailed in Appendix A. Although the physical domain is quite industrially realistic, compromises had to be made regarding the simplified single-step chemical model used and the moderate operating conditions achieved.

Utilizing multi-step chemistry mechanisms, while more accurate, allows for the dependency of both pressure and temperature on the flame width. This pressure dependency in

these highly compressible regimes thins the flame width and further exacerbates the tyranny of scales issue. While multi-step chemical models can be employed, alternative compromises of the physical domain are often required. One such study, detailed in Appendix B, was carried out using a multi-step chemical mechanism for n-dodecane fuel at very high turbulent regimes. Many other previous studies have explored similar or somewhat more moderate turbulent regimes in similar, idealized domains.

Simplified Physical Systems

An extensive series of simplified "flame in the box" simulations in driven Kolmogorov-type turbulence have laid the groundwork for the study of reacting turbulence in realistic flows. These studies characterized the structure, speed, and unconfined transition to detonation of turbulent flames.

Flame Structure

Turbulent flow fields and intrinsic instabilities cause laminar flames to become distorted by turbulent motions soon after ignition. The resulting turbulent flame brush eventually reaches a quasi-steady state of reasonably constant width and speed. In the preheat zone ahead of the flame, turbulent motions affect the flow on small scales, wrinkling the flame front considerably. However, the flame surface remains relatively smooth at the higher temperatures on the product side [9]. Turbulent intensity affects the local flame orientation, the width of the preheat and reaction zones, as well as the scalar dissipation. Vorticity and strain rate, both measures of local turbulence structure within the flow, are not considerably affected by the reaction zone of the flame at lower Karlovitz numbers [10, 11]. Lagrangian analysis shows that high speed turbulence substantially alters the chemical composition and temperature evolution of fluid parcels in single-

and multi-step chemistry simulations and introduces significant nonmonotonicity of the thermochemical trajectories [12].

Ahead of the flame brush, net energy transport is from large to small scales, however, transfer of energy upward from the smallest scales can occur within the flame brush, where thermal expansion injects significant amounts of energy at these small scales [13]. This is seen in both statistically planar [14] and three-dimensional turbulent premixed flames [15].

Flame Speed

In the thin reaction zones regime, where turbulent intensity is high, the distortion of the turbulent flame front gives rise to cusp formation and flame collisions as the flame propagates. Turbulent flame burning speeds can be determined predominantly from the increase of the flame surface area, as the flame wrinkles and folds upon itself. Although these effects of turbulence induce considerably larger flame speeds than could be expected from a laminar flame, the inability of turbulence to penetrate the reaction zone itself implies that the turbulent burning speed is not decoupled from the laminar flame speed at the intensities considered [16]. Turbulent deflagrations can form leading compression waves or shocks ahead of the flame front. At sufficient intensities, these deflagrations can transition to another type of reaction wave, known as a detonation, as discussed below. [17, 18]

Deflagration-to-Detonation Transition

Detonations have the potential to advance the next-generation propulsion technology through the implementation of detonation engines [19, 20]. In this context, the onset of a detonation through DDT has been the subject of much study. Although some control of detonation onset is possible [21, 22], the physical mechanisms giving rise to DDT remain poorly understood.

Much of the theory of DDT has developed in the context of confined systems, where detonations form in regions of high temperature and reactivity gradients [23]. While it has long been known how these non-uniformities can form in confined flows [17], DDT in unconfined flows has proven more difficult to study [24-26]. However, under the right conditions, unconfined DDT is thought to play a part in massively powerful phenomena, such as large vapor cloud and Type Ia supernovae (SNIa) explosions [27-30].

Prior flame in the box simulations have shown that unconfined DDT can be onset by pressure buildup caused by flame-turbulence interactions [31]. Chapman-Jouguet (CJ) theory defines S_{CJ} as the theoretical maximum speed of a steady-state laminar flame [32, 33]. However, fast turbulent flames can self-accelerate to detonation in a catastrophic runaway process as the turbulent flame burning speed, S_T, surpasses S_{CJ},

$$S_T \geq S_{CJ} = \frac{c_s}{\alpha}, \qquad \alpha = \frac{\rho_F}{\rho_p},$$

where c_s is the speed of sound in the hot reaction products and α is the ratio of densities in the fuel, ρ_F, and products, ρ_p [9].

Simplified Chemistry

Fully exploring the flow physics of these extreme regimes requires examining all sides of the previously proposed dilemma. This thesis will explore a complex, experimentally realistic physical system, capable of achieving extreme turbulent reacting flow regimes, while employing a simplified single-step reaction model.

Chapter II provides an overview of the numerical solver, Athena-RFX, including the chemical reaction model. Chapter III details the experimental facility which we aim to represent with DNS. Chapter IV further describes the imposed boundary conditions and configuration of the DNS, designed to best replicate the Turbulent Shock Tube (TST). Chapter V examines the flow

evolution of a TST cycle as seen in the numerical simulation. Chapter VI analyzes and identifies the regimes achieved. Chapter VII highlights how the flame behaves in these regimes, namely, key aspects of flame speed measurements, both numerically and experimentally. Chapter VIII discusses the source of the large flame and turbulent velocities observed, particularly via flame driven turbulence generation. Finally, Chapter IX concludes with a summary of findings.

While the main content of this thesis is aimed at advancing the research of experimentally realistic, extreme reacting flow regimes, Appendix A will discuss an industrially realistic combustor configuration, the PRECCINSTA swirl combustor, and Appendix B will touch upon high Karlovitz number flame in the box simulations performed with detailed, multi-step chemical models.

CHAPTER II

NUMERICAL SOLVER

The simulations herein have been performed using the Athena-RFX code, which uses a fully unsplit, corner-transport upwind scheme with PPM spatial reconstruction and an HLLC Riemann solver [34, 35]. Several previous [9-12, 16, 31, 36] studies of turbulent combustion have utilized this code and discuss the numerical solver and convergence tests in detail. Athena-RFX solves the unsteady, compressible reactive Navier-Stokes equations:

$$\frac{\partial \rho}{\partial t} + \nabla \cdot (\rho \boldsymbol{u}) = 0, \tag{1}$$

$$\frac{\partial \rho \boldsymbol{u}}{\partial t} + \nabla \cdot (\rho \boldsymbol{u} \otimes \boldsymbol{u}) + \nabla P + \nabla \cdot \hat{\tau} = 0, \tag{2}$$

$$\frac{\partial E}{\partial t} + \nabla \cdot \big((E + P)\boldsymbol{u}\big) + \nabla \cdot (\boldsymbol{u} \cdot \hat{\tau}) + \nabla \cdot (\mathrm{K} \nabla T) + \rho q \dot{w} = 0, \tag{3}$$

$$\frac{\partial \rho Y}{\partial t} + \nabla \cdot (\rho Y \boldsymbol{u}) + \nabla \cdot (\rho D \nabla Y) - \rho \dot{w} = 0. \tag{4}$$

Here ρ is mass density, $\boldsymbol{u}$ is velocity, E is energy density, P is pressure, T is temperature, Y is fuel mass fraction, q is chemical energy release rate, $\dot{w}$ is the reaction rate, and $\hat{\tau}$ is the viscous stress tensor,

$$\hat{\tau} = \rho \nu \left(\frac{2}{3} (\nabla \cdot \boldsymbol{u}) \boldsymbol{I} - (\nabla \boldsymbol{u}) - (\nabla \boldsymbol{u})^{\dagger} \right), \tag{5}$$

where ν is the kinematic viscosity, $\boldsymbol{I}$ is a unit matrix, and † indicates a matrix transposition. The coefficients of thermal conduction, K, and molecular diffusion, D, are assumed to have the same temperature dependence,

$$\mathrm{K} = \kappa_0 C_p T^n, \;\; D = D_0 T^n / \rho, \tag{6}$$

where $C_p = \frac{\gamma R}{M(\gamma - 1)}$ is the specific heat at constant pressure and the Lewis number, $Le = \frac{\kappa_0}{D_0} = 1$ is independent of the thermodynamics of the flow.

The equation of state is taken as that of an ideal gas and chemical reactions are modeled using simplified single-step, first-order Arrhenius kinetics:

$$\frac{dY}{dt} \equiv \dot{w} = -A\rho Y e^{-\frac{Q}{RT}} \tag{7}$$

where A is the pre-exponential factor, Q is the activation energy, and R is the universal gas constant.

Table 1 summarizes the input model parameters for the simplified reaction model of the stoichiometric H_2-air mixture used. These model parameters have been calibrated to reproduce experimental laminar flame speed and width, as well as detonation speed and half reaction width [37, 38]. To match these flame and detonation properties, some of the adjustable parameters, such as the adiabatic index, γ, have deviated significantly from their actual values. In light of this, future work may implement a single or multi-step chemical model which is able to more realistically match the adjustable parameters.

Table 1 Input model parameters for single-step H_2-air model

T_0	293 K	Initial reactant temperature
P_0	$1.01 \times 10^6 \mathrm{erg/cm^3}$	Initial reactant pressure
ρ_0	$8.73 \times 10^{-4}\ \mathrm{g/cm^3}$	Initial reactant density
M	$21\ \mathrm{g/mol}$	Molecular weight (H2-air)
γ	1.17	Adiabatic index
n	0.7	Temperature exponent
μ_0	$3.1 \times 10^{-6}\ \mathrm{g/(s \cdot cm \cdot K^n)}$	Viscosity coefficient
κ_0	$2.9 \times 10^{-5}\ \mathrm{g/(s \cdot cm \cdot K^n)}$	Conduction coefficient
D_0	$2.9 \times 10^{-5}\ \mathrm{g/(s \cdot cm \cdot K^n)}$	Diffusion coefficient
Q	$46.37\mathrm{RT_0}$	Activation energy
A	$6.85 \times 10^{12}\ \mathrm{cm^3/(g \cdot s)}$	Pre-exponential factor
q	$43.28\,\mathrm{RT_0/M}$	Chemical energy release
δ_L	$0.032\ \mathrm{cm}$	Laminar flame thermal width
S_L	$302\ \mathrm{cm/s}$	Laminar flame speed

CHAPTER III

TURBULENT SHOCK TUBE FACILITY

The Turbulent Shock Tube (TST) developed at the University of Central Florida by the Propulsion and Energy Research Laboratory (PERL) is designed to study high-speed flames in highly compressible regimes including detonations, and at conditions close to DDT. The semi-confined 4.5×4.5 cm square channel shown in Figure 1 consists of an igniter, a turbulence generation section, and a diagnostic section.

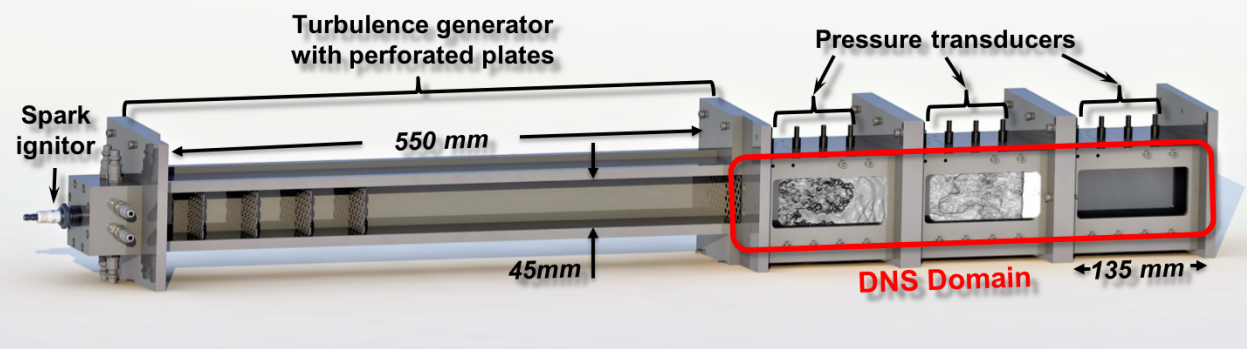

Figure 1 Turbulent Shock Tube (TST) Facility.

Operation

The TST can probe a wide range of combustion modes, from deflagrations to detonations. The 150 cm long shock tube is initially filled with premixed Hydrogen-air fuel over a period of 20 seconds. The mixture is allowed to settle for 3 seconds before the spark ignitor at the axial center of the closed end is triggered. A flame kernel forms, quickly expands to fill the transverse dimension of the shock tube, and begins to propagate toward the open end of the tube. The turbulence generator section contains a series of 5 plates with 6.35 mm diameter perforations which disrupt the flame and cause rapid acceleration via turbulence. This flame acceleration eventually forms a leading shock and another highly compressed region of fuel ahead of the flame.

One final perforated plate is situated immediately ahead of the diagnostic section so that choked, turbulent jets generate high levels of quasi-isotropic turbulence in the post-shock flow. Only the diagnostic section is represented in the DNS. Measurements and diagnostics are taken in the optically accessible sections of the TST. At the end of the diagnostic section, the flow is vented into atmospheric conditions.

Diagnostics

The interaction of the flame with high-speed turbulence is examined using a combination of techniques, including high speed schlieren imaging, chemiluminescence, and high-speed PIV. Additionally, an array of transducers along the diagnostic section provides pressure evolution data.

High speed schlieren is used to characterize flame and shock behavior within a diagnostic window at a recording rate of 100 kHz and a spatial resolution of 175 μm/px. This can be compared to a "synthetic schlieren" (density gradient magnitude in a plane) from the DNS.

High speed particle image velocimetry (PIV), recorded at 20 kHz, is used with simultaneous 40 kHz OH* chemiluminescence to determine flame flow conditions used in the calculation of flame speed and in-depth analysis of the turbulent flow field. The PIV uses 20 μm aluminum oxide particles uniformly seeded within the domain. It has a spatial resolution of 40 μm/px, a particle image diameter to pixel size of about 1.5, and a velocity uncertainty of less than 5 m/s. The OH* chemiluminescence provides images of the instantaneous flame front which can be superimposed on the PIV. The chemiluminescence has a spatial resolution of 156 μm/px. Additional thermodynamic quantities are calculated using normal shock relations across the leading shock and isentropic relations behind the shock along with the ideal gas law and the NASA Chemical Equilibrium with Applications code.

A series of four pressure transducers spaced 25 mm apart along the test section centerline provide pressure profiles at a rate of 250 kHz with an uncertainty of ± 0.17 atm. These transducers, indicated in Figure 1, are centered in the transverse direction. The DNS can compare these pressure signals to pressure data in the same locations at the wall of the DNS domain averaged over an effective sensor area of 0.25×0.25 cm.

Experimental Findings

Previous work by PERL has extensively studied the channel configurations needed to achieve reliable and repeatable control of the flow dynamics [21, 22]. The turbulent intensity, and by extension the combustion regime for a cycle, is controlled by the equivalence ratio. Equivalence ratios are chosen such that the flow regime of interest is observable within the diagnostic section.

Using the equivalence ratio as a control parameter, the TST can explore the entire range of combustion modes including turbulent fast flames, detonations, and flames coupled to a shock but not yet within the detonation regime [21]. This experimental research has observed flame interaction with shock-driven isotropic turbulence, flame turbulence generation, and the turbulence-based runaway mechanism for turbulent DDT based on the turbulent flame speed and the CJ deflagration speed criteria [22, 39, 40].

Figure 2 summarizes peak pressure and speed measurements within the first diagnostic segment over a wide range of equivalence ratios. Flame speed is closely tied to the turbulent intensity, and thus the equivalence ratio. These turbulent flame speeds, reported as S_T, are experimentally measured flame displacement speeds, normalized by S_{CJ}. Pressures within the flame are highly sensitive to equivalence ratio and begin to run away as S_T becomes larger than S_{CJ}. [40]

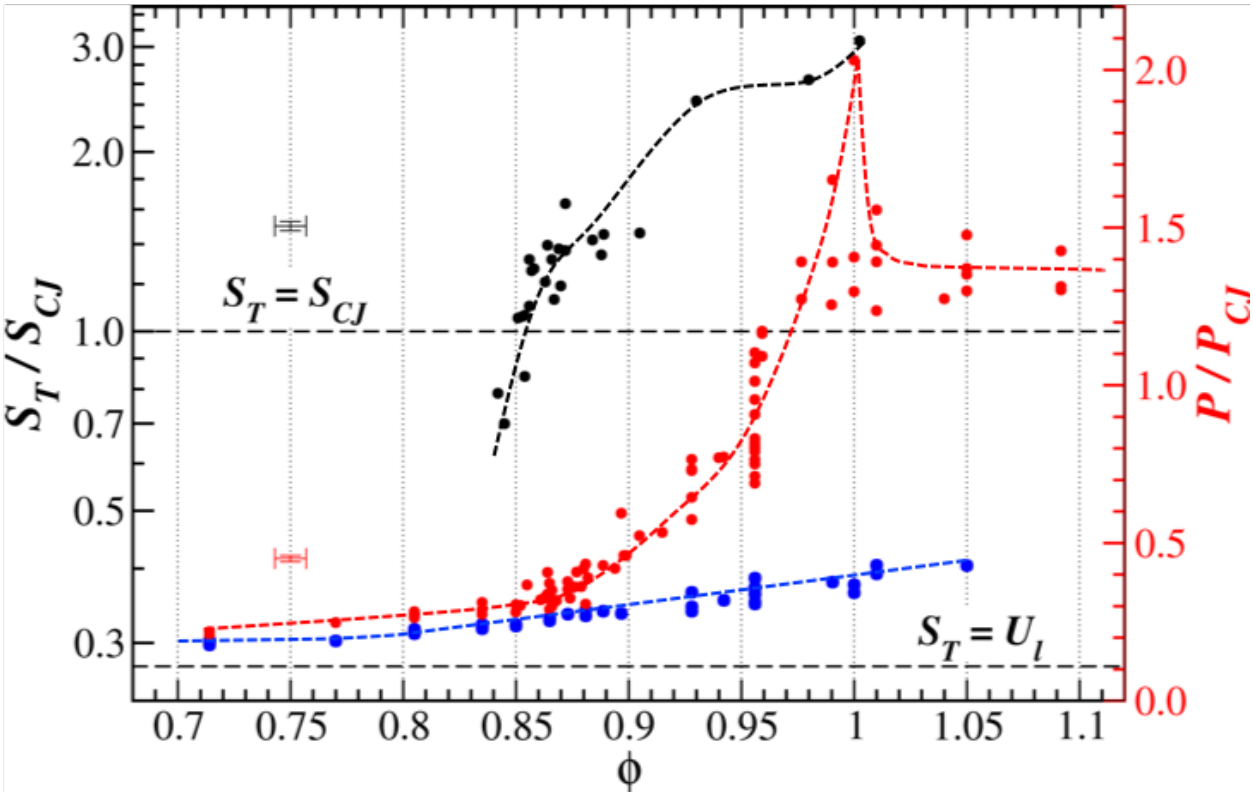

Figure 2 Pressure and turbulent flame velocities observed in the TST over a range of equivalence ratios [40]. Black points indicate turbulent flame displacement speeds at the beginning of the diagnostic section scaled by S_{CJ}, while red and blue points show peak pressures generated by the flame in the first segment of the diagnostic section and peak pressures of the global shock after it passes through the last perforated plate, respectively.

CHAPTER IV

DNS CONFIGURATION

Extensive effort was made to maintain realistic boundary conditions in the numerical simulation. The 4.5×45 cm walls of the channel are no-slip, adiabatic walls, and the outlet boundary condition is a zeroth-order extrapolation outflow. The inlet boundary condition represents the last perforated plate of the turbulence generation section. The solid sections are a no-slip wall with a pattern of orifices shown in Figure 3, which inject fuel (or product after the flame has passed) according to a prescribed pressure evolution.

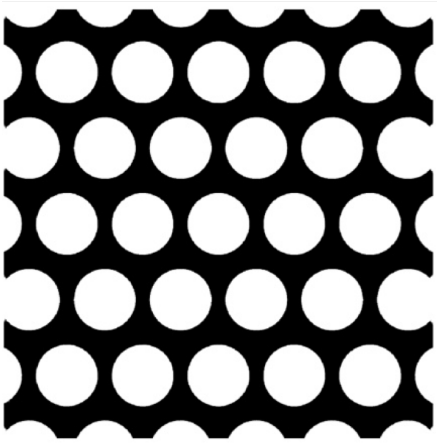

Figure 3 Orientation of perforated plates in the turbulence generator section.

The injection flow evolution is complex and not directly accessible in the experimental configuration. Neither the experimental nor numerical studies analyze flow within the turbulence generation segment of the TST, which motivated the installation of a pressure transducer on the upper wall of the TST centered 0.625 mm upstream of the last perforated plate. This transducer signal provides some insight into the experimental flow field immediately prior to the diagnostic section, near the injection plane. The pressure trace of a representative experimental run is shown as T0 in Figure 4.

A smoothed version of this data, shown as DNS Injection Pressure in Figure 4, is used as a time evolution of the injection pressure profile within the plate perforations. Flow through the orifices is assumed to be choked and remaining flow properties, such as temperature and velocity, are calculated using isentropic relations. During the injection of the flame itself, thermodynamic properties along a laminar flame profile relative to the prescribed pressure injection profile are followed to avoid an abrupt transition from fuel to product injection. This T0-based injection pressure profile is able to reasonably reproduce subsequent transducer pressure profiles within the diagnostic section as detailed in Chapter V.

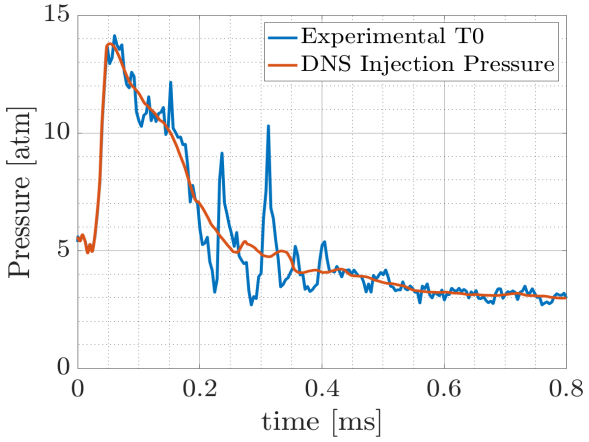

Figure 4 Experimental transducer pressure data ahead of the diagnostic section and DNS injection pressure profile.

Experimentally, as equivalence ratio is increased, more energy is released during combustion, leading to higher turbulent intensities and pressures. The DNS is calibrated to probe particular flow conditions by directly rescaling the pressure input profile. This provides similar control of the turbulent flame speed and intensity as the equivalence ratio in the experimental facility described in Chapter III. This numerical pressure scaling factor exhibits a highly nonlinear sensitivity, also seen in the ϕ dependency of standing flames at highly compressible regimes in the experimental TST facility [41]. DNS cases with injection pressure scaling factors of 1.0 and

0.9 transitioned to detonation prior to the flame moving sufficiently past the injection region. Future work will focus on turbulent intensity tuning in the DNS setup using this scaling factor, and analyzing the entire range of reacting combustion modes, from simple deflagrations to DDT.

In the following chapters, data from two different DNS will be analyzed; these are detailed in Table 2. These cases differ in their resolution and allow us to assess convergence.

Table 2 Numerical simulation parameters

Case	Resolution	Injection Pressure Scaling Factor	dx/δ_L	Core Count	Completion Time
P08	1024x1024x10240 cells	0.8	7.37	~16k	~3 weeks
P08h	2048x2048x20480 cells	0.8	14.73	~32k	~3 months

CHAPTER V

FLOW EVOLUTION

Turbulent shock tube operation begins with ignition of a flame kernel. Once initiated, the flame propagates away from the ignition source as a deflagration via heat and mass diffusion. Turbulence is generated from the flow disruptions caused by the perforated plates. This turbulence drives a rapid acceleration of the flame and causes a high-pressure, compressed region to be formed ahead, eventually leading to the formation of a coupled shock wave ahead of the reaction wave. The numerical simulation begins as the flow is sent through the last perforated plate and a Mach ~2 shock enters the diagnostic section.

Figure 5 shows the distribution of various spanwise-averaged quantities along the direction of flame propagation at several time instants for case P08h. The corresponding evolution data for case P08 showed extremely close agreement to the higher resolution case. The pressure profiles in Figure 5 show the location of the leading shock as the jump from 1 atm to $4-5$ atm. This leading shock decays slightly over time, but remains about Mach 2. Also visible in the pressure evolution is the compressed region ahead of the flame. Initially narrow, this pre-flame compressed region forms a second shock ahead of the reaction zone. Consistent with normal shock theory, this trailing shock approaches and eventually overtakes the leading shock. The resulting leading shock after collision is closer to Mach 3. The shock collision causes a rarefaction wave to propagate back through the flow relative to the flame.

From the profiles of velocity fluctuations in Figure 5, it can be seen that, while turbulent intensity is significant immediately downstream of the perforated plate, it decays rapidly as the flow propagates through the domain. However, subsequent time instants show that turbulent intensity proceeds to increase in and behind the flame, reaching levels of ~80-100 m/s for

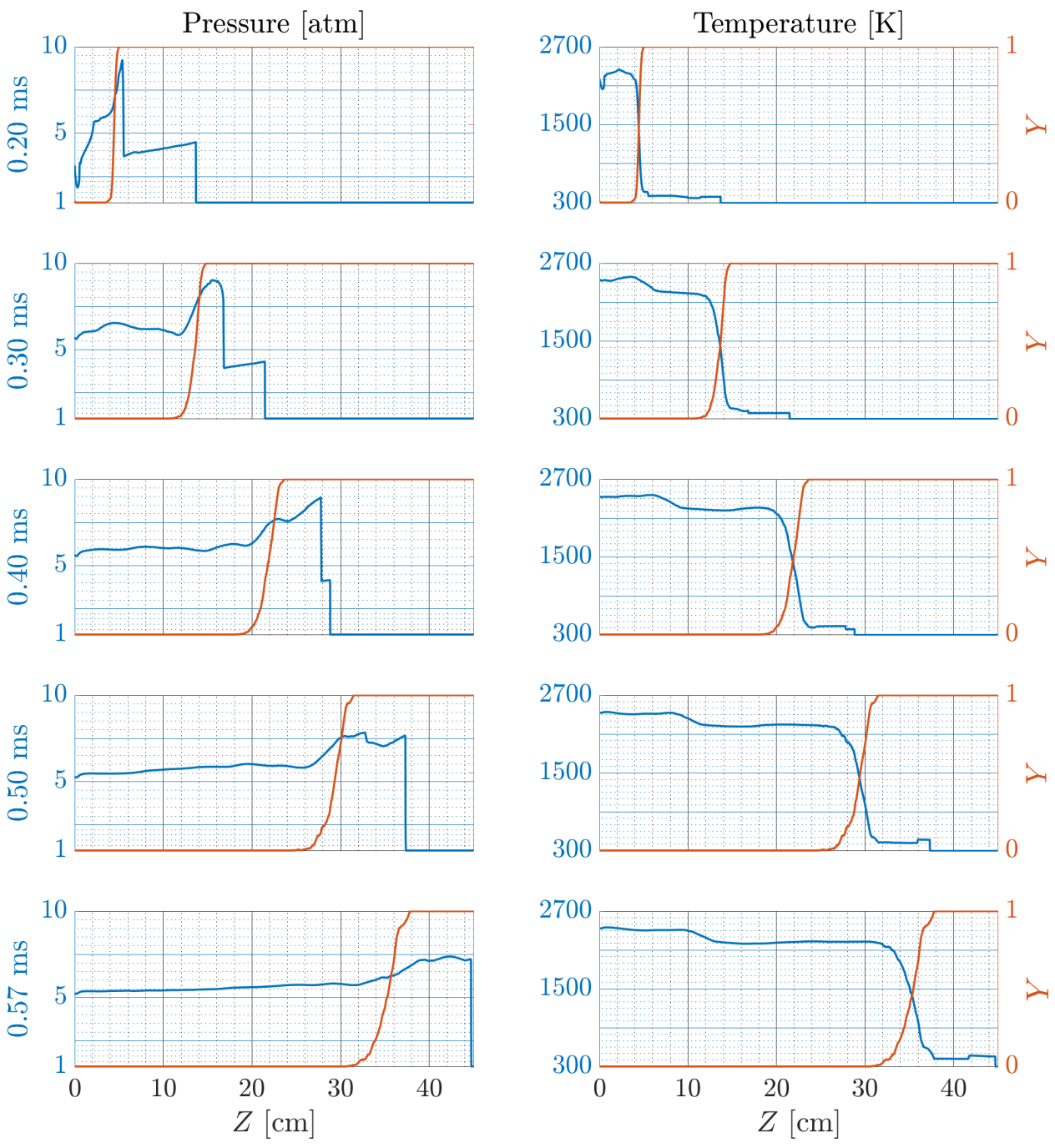

Figure 5 Flow evolution of thermodynamic quantities and speeds for Case P08h with the location of flame indicated by the fuel mass fraction.

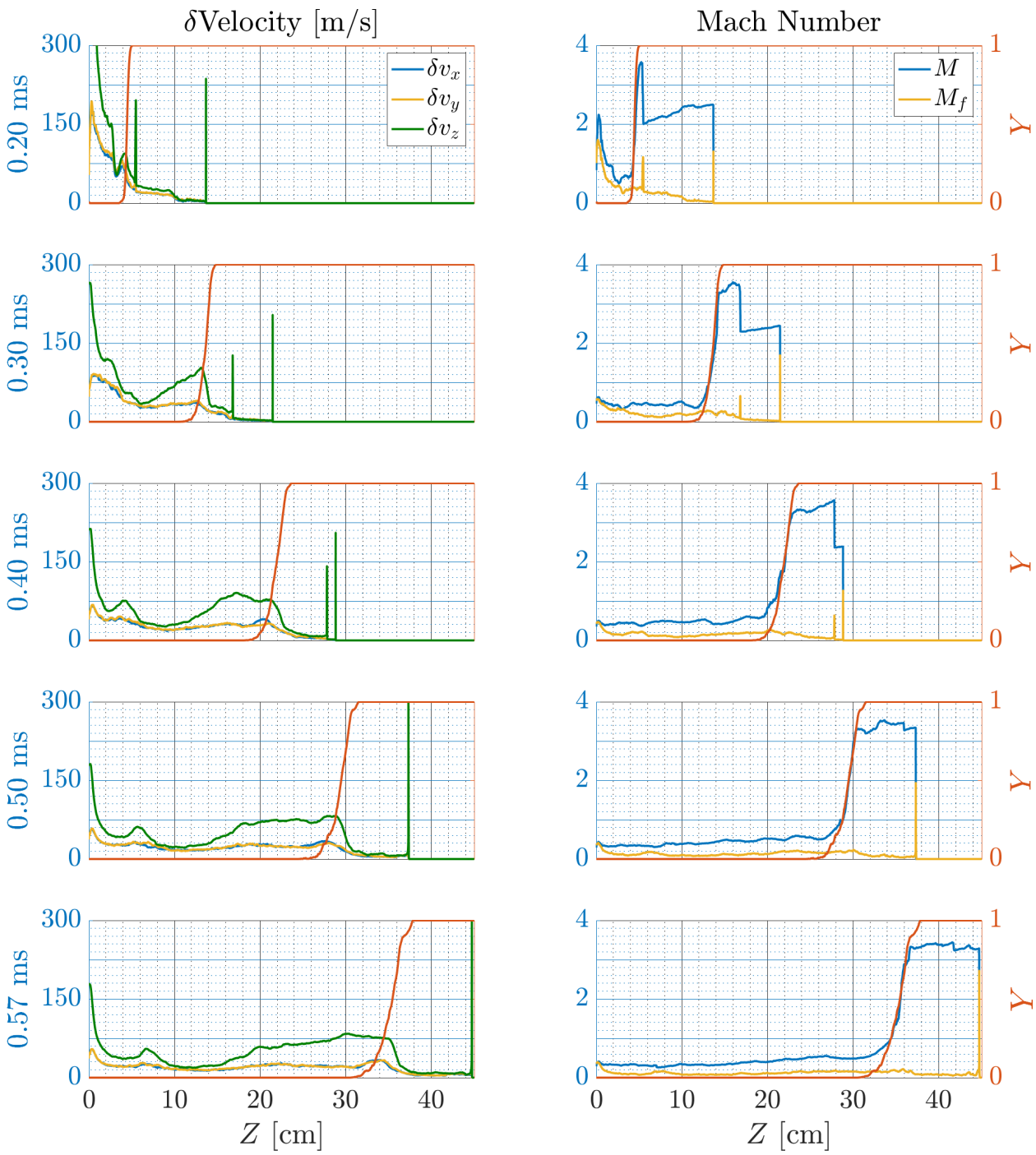

Figure 5 Continued.

streamwise velocity fluctuations and ~30-40 m/s for the spanwise fluctuations. Such flame-generated turbulence was previously observed in the more idealized flame in the box calculations with driven homogeneous isotropic turbulence [31], and this DNS provides the first indication of the presence of such turbulence-generation mechanism in a realistic flow, without external turbulence driving. Finally, the Mach number based on local velocity components is driven to supersonic speeds between Mach $3-4$ ahead of the flame over the simulation time, while the fluctuating Mach number maintains a spanwise average of $0.2-0.4$ around the flame. The coupling of the shock and reaction waves exhibited here classifies this reaction as a shock-flame complex.

Pressure Transducers

As detailed in Chapter III, the experimental TST provides pressure transducer signals for four locations along the axial direction of the diagnostic section. These are located 4.0034 cm, 6.8028 cm, 9.6022 cm, and 12.4016 cm from the injection plane. By taking a small area average of the pressure field at the same domain locations during the DNS, we are able to compare the numerical and experimental flows as they progress through the domain. The effective sampling area is 0.25×0.25 cm, centered at the axial transducer location and the midsection of the y-dimension. This orientation aligns the transducers with the top center of the perforated plate in Figure 3. Figure 6 shows the comparison of the DNS cases to an experimental run of similar leading shock intensity. The initial pressure jump, from 1 atm to $4-5$ atm, is due to the passage of the leading shock. Pressure decays behind the shock until the flame and preceding compressed region reach each transducer, causing another notable pressure spike and subsequent large pressure fluctuations due to turbulence and reflected shocks behind the flame. Finally, pressure decays as cooler products pass.

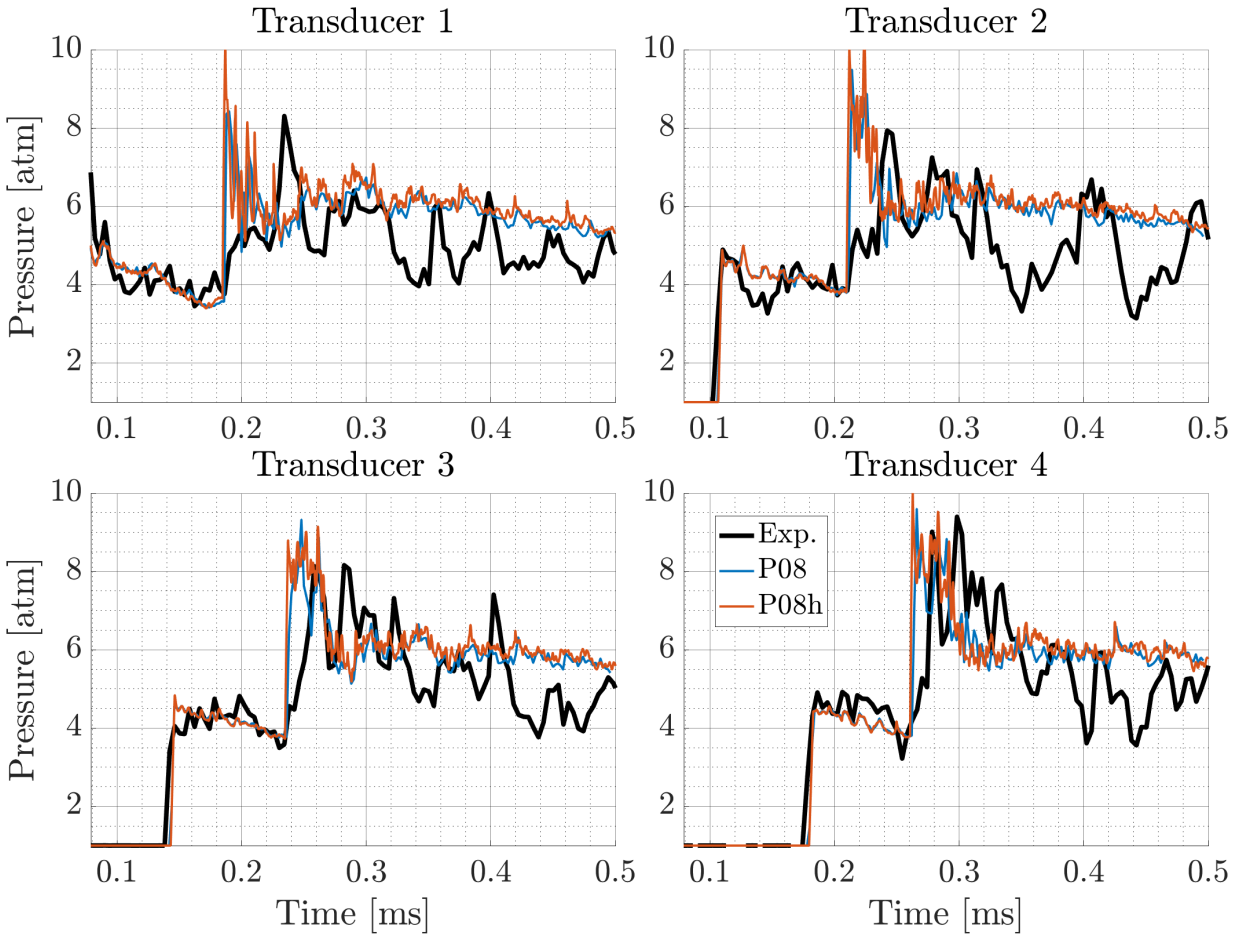

Figure 6 Pressure transducer signal from the experimental run and synthetic transducer signals from DNS for all simulation test cases.

Agreement between both DNS cases is excellent and the numerical and experimental signals are comparable, especially in the region behind the leading shock. The lack of an immediate, sharp pressure jump ahead of the flame in the experimental signal early in the domain indicates that this flame propagated as a fast deflagration prior to transitioning to a shock-flame complex. This is further supported by the evolution of the flame in P-V space.

PV Evolution

Figure 7 shows the flame averaged pressure and specific volume over time between the Hugoniot and shock adiabat. Unlike a detonation, which is characterized by a drop in specific

volume and a rise in pressure, the TST flame at this pressure scaling factor exhibits an overall decrease toward the deflagration solution. Towery characterizes this type of evolution as a quasi-constant pressure ignition [42].

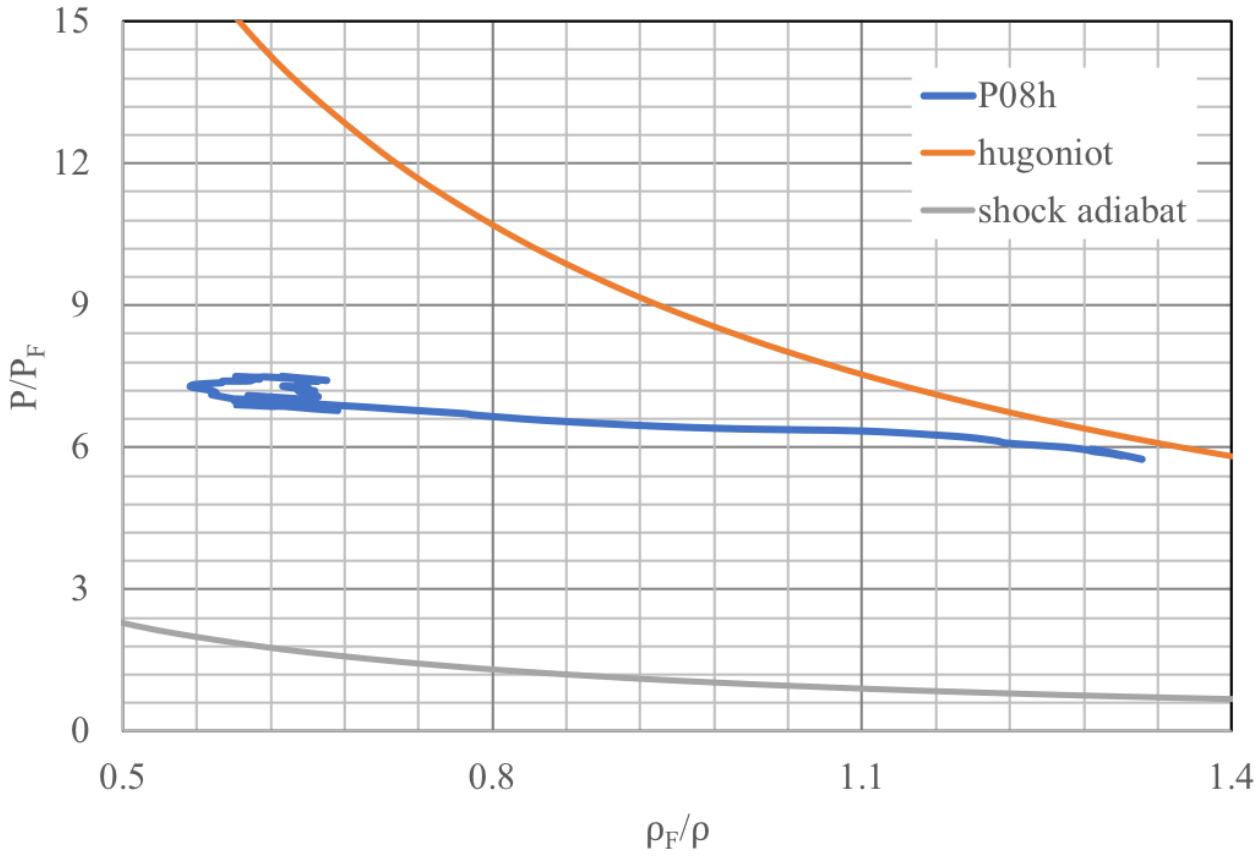

Figure 7 Evolution of the flame for case P08h in PV space, normalized with initial cold fuel pressure and density.

Flow Subdomains

For analysis purposes, subdomains (SDs) are assigned within the full domain based on the flow conditions. The spanwise-averaged pressure $\bar{P}$, and fuel mass fraction $\bar{Y}$ are used to set the limits of each region. In total, 8 SDs are set, including the product region (SD-P), the highly compressed fuel ahead of the flame (SD-C), the fuel compressed by the leading global shock but ahead of the flame-generated shock (SD-S), and 5 SDs within the flame based on $\bar{Y}$ (SD-F1-5).

Figure 8 shows a 2D pseudocolor plot of pressure with the $\bar{P}$ and $\bar{Y}$ overlaid, and the location of the subdomains for one instant. The axis labels (in cm) and colormap (in atm) in Figure 8 correspond to the pseudocolor plot. The transverse averages share the same x-axis (z-coordinates) with the pseudocolor plot, while the y-axis ranges from 0 to 10 atm for pressure and 0 to 1 for fuel mass fraction.

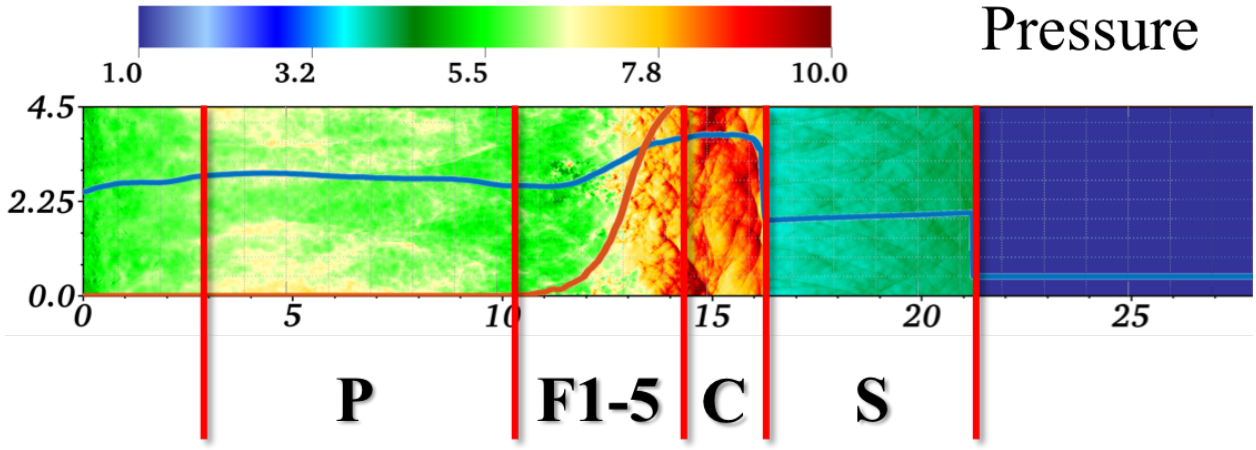

Figure 8 Subdomain division shown on a pseudocolor plot of pressure and overlaid transverse-averaged plots of pressure and fuel mass fraction.

For all regions to be present and reasonably developed, analysis involving SDs can only be considered after the front of the flame passes 4 cm in the axial direction. The lower limit of SD-P is set at 3 cm, such that the effects of the highly turbulent injection jets are excluded. The upper limit of SD-P is defined by the back of the flame brush ($\bar{Y} < 0.001$). The flame SDs cover equal ranges of $\bar{Y}$ values with the lower limit of SD-F1 at $\bar{Y} \geq 0.001$ and the upper limit of SD-F5 at $\bar{Y} < 0.999$. The first compressed region ahead of the flame, SD-C, is bounded by the front of the flame brush ($\bar{Y} \geq 0.999$) and the flame-generated shock. Finally, SD-S, is the region ahead of the flame-generated shock but behind the leading shock.

CHAPTER VI

ANALYSIS

UCF's TST facility and this numerical study have been developed to study strongly compressed, high-speed, highly turbulent flame regimes. Using this coupled computational study, we can quantify the extent of the regimes achieved in this configuration.

Combustion Regimes

Standard combustion regime diagrams, such as the classical Borghi diagram [43], characterize flow with a length scale and velocity scale both normalized with laminar values. This regime diagram categorizes conditions into laminar flames, wrinkled flamelets, corrugated flamelets, thin reaction zones, and broken reaction zones. Karlovitz and Damkholer numbers, along with a related turbulent Reynolds number, correspond to the boundaries of these zones. These three non-dimensional quantities are not independent, but related by the Kolmogorov hypothesis [44] as

$$Da\,Ka = Re^{1/2}. \tag{8}$$

The length and velocity scales which these diagrams are constructed from depend on the turbulent velocity fluctuations, δu_i, which are the differences between the local velocity components, u_i, and the transverse-averaged velocity components at that streamwise coordinate, $\langle u_i \rangle_{x,y}$,

$$\delta u_i = u_i - \langle u_i \rangle_{x,y}. \tag{9}$$

First, the integral velocity scale, u', is defined as the "single-component root mean square"

$$u' = \sqrt{\frac{\delta u_i \delta u_i}{3}}. \tag{10}$$

Then, the integral length scale, ℓ', is determined using the equation for Kolmogorov-type turbulence based on (10), the energy dissipation rate, $\varepsilon = 2\nu\overline{s_{ij} \cdot s_{ij}}$, the kinematic viscosity, ν, and the strain rate s_{ij},

$$\ell' = \frac{1}{2}\frac{u'^3}{\varepsilon}. \tag{11}$$

The integral length scale is much larger than the simulation cell size and thus has no meaning when calculated at the cell scale. Instead, we consider integral scales u' and ℓ' as SD volume-averaged quantities. The integral velocity scale is then, explicitly,

$$\langle u' \rangle_V = \sqrt{\frac{\Sigma\left(\frac{\delta u_1 \delta u_1}{3} + \frac{\delta u_2 \delta u_2}{3} + \frac{\delta u_3 \delta u_3}{3}\right)}{N\ cells \in SD}}. \tag{12}$$

For the ℓ', a volume averaged ε is used as well,

$$\langle \ell' \rangle_V = \frac{1}{2}\frac{\langle u' \rangle_V^3}{\langle \varepsilon \rangle_V}. \tag{13}$$

Regime diagrams based on integral velocity (12) and length (13) scales for a developed flame in both TST DNS are shown in Figures 9 and 10, plotted over a time range from $0.2 - 0.57$ ms. The colormaps correspond to the simulation time. Nonreacting flow SDs are shown in Figure 10, while the flame SDs (and SD-C) are shown in Figure 9. These regimes generally agree with those that have been experimentally obtained in the TST for fast, highly turbulent standing flames [41]. While P08 appears to achieve ℓ'/δ_L up to 1000, the P08h run is shifted toward lower ℓ'/δ_L, within the thin reaction zones regime between $1 > Ka > 100$. Although this leftward shift may indicate that P08h is still not adequately resolved, the situation may be more nuanced. The integral length scale is based on (13) which involves ε and u'. The integral velocity scales appear sufficiently converged, and the differences in ε will be discussed shortly. However, there is no fundamental reason that the energy dissipation rate should depend on the integral length scale for

this flow, as ℓ' is not the scale at which energy dissipates, and the assumption of Kolmogorov-type turbulence is only loosely applicable here. Further exploration of energy dissipation rates on different scales could determine a more appropriate ε and resolve some of the discrepancy.

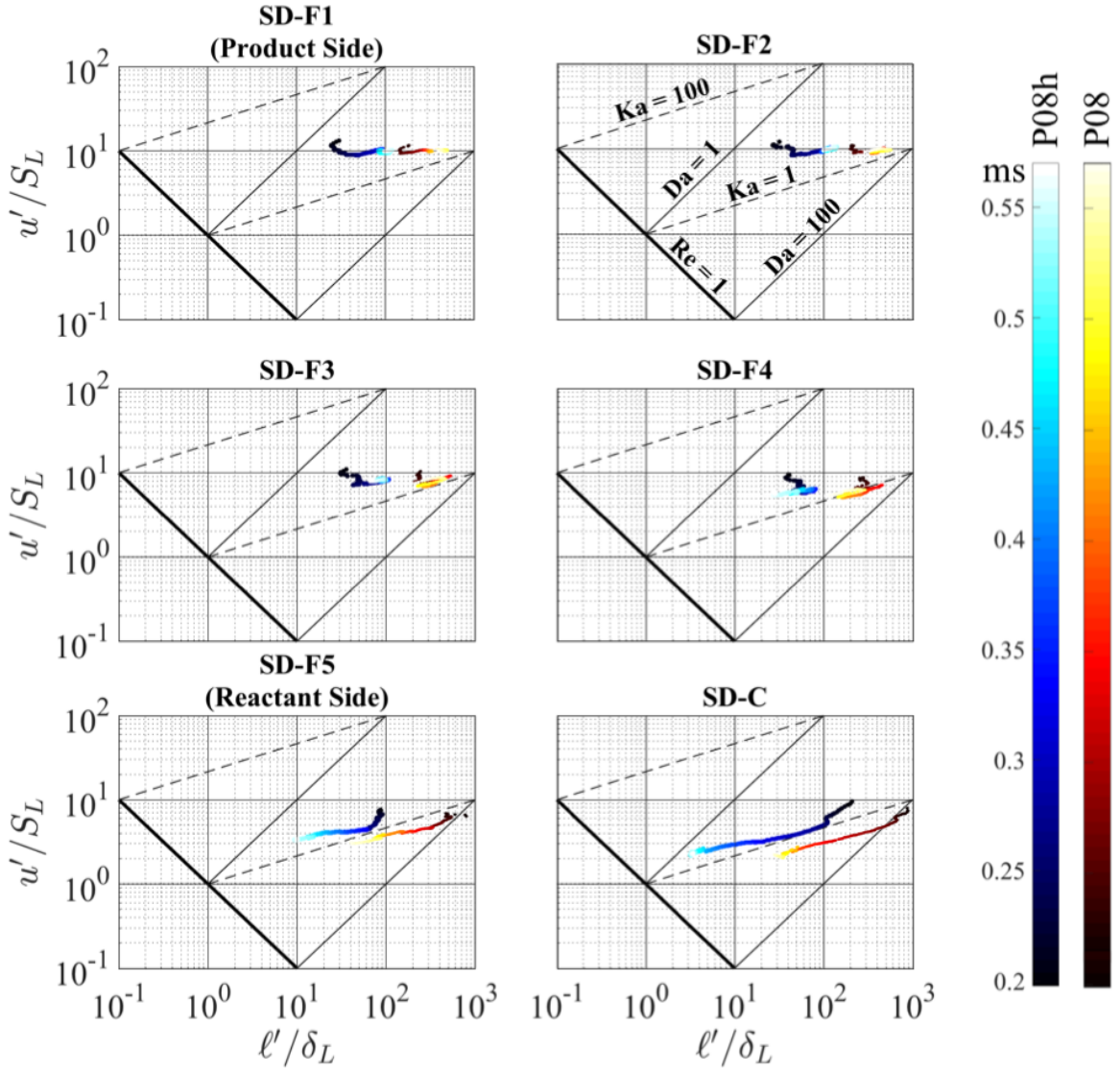

Figure 9 Regime diagram evolution for flame SDs and SD-C over relevant simulation time with laminar flame values based on temperature immediately ahead of the flame brush for case P08h (blue) and P08 (red).

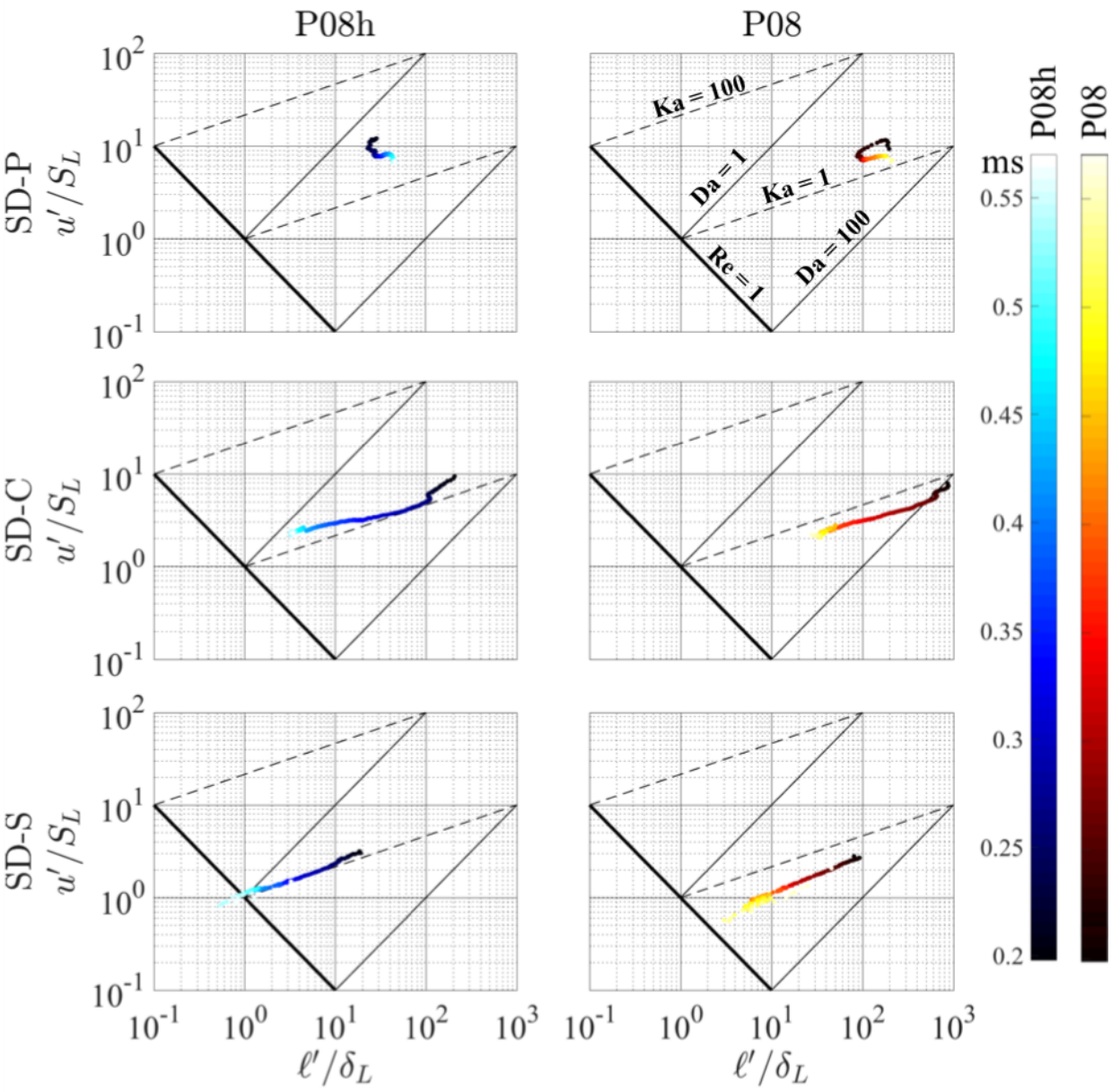

Figure 10 Regime diagram evolution for nonreacting SDs over relevant simulation time with laminar flame values based on temperature immediately ahead of the flame brush for case P08h (blue) and P08 (red).

Compared to other studies in the Navy Research Lab (NRL) and Texas A&M Databases, the TST achieves large length scales at moderately high velocity scales, especially within the flame regions, SD-C, and SD-P. This is illustrated in Figure 11. While the flame in the box studies are capable of probing high Karlovitz numbers, they tend to be limited to small or moderate length

scales. Additionally, these previous studies lacked a realistic setting, and turbulence was driven at large scales within the domain.

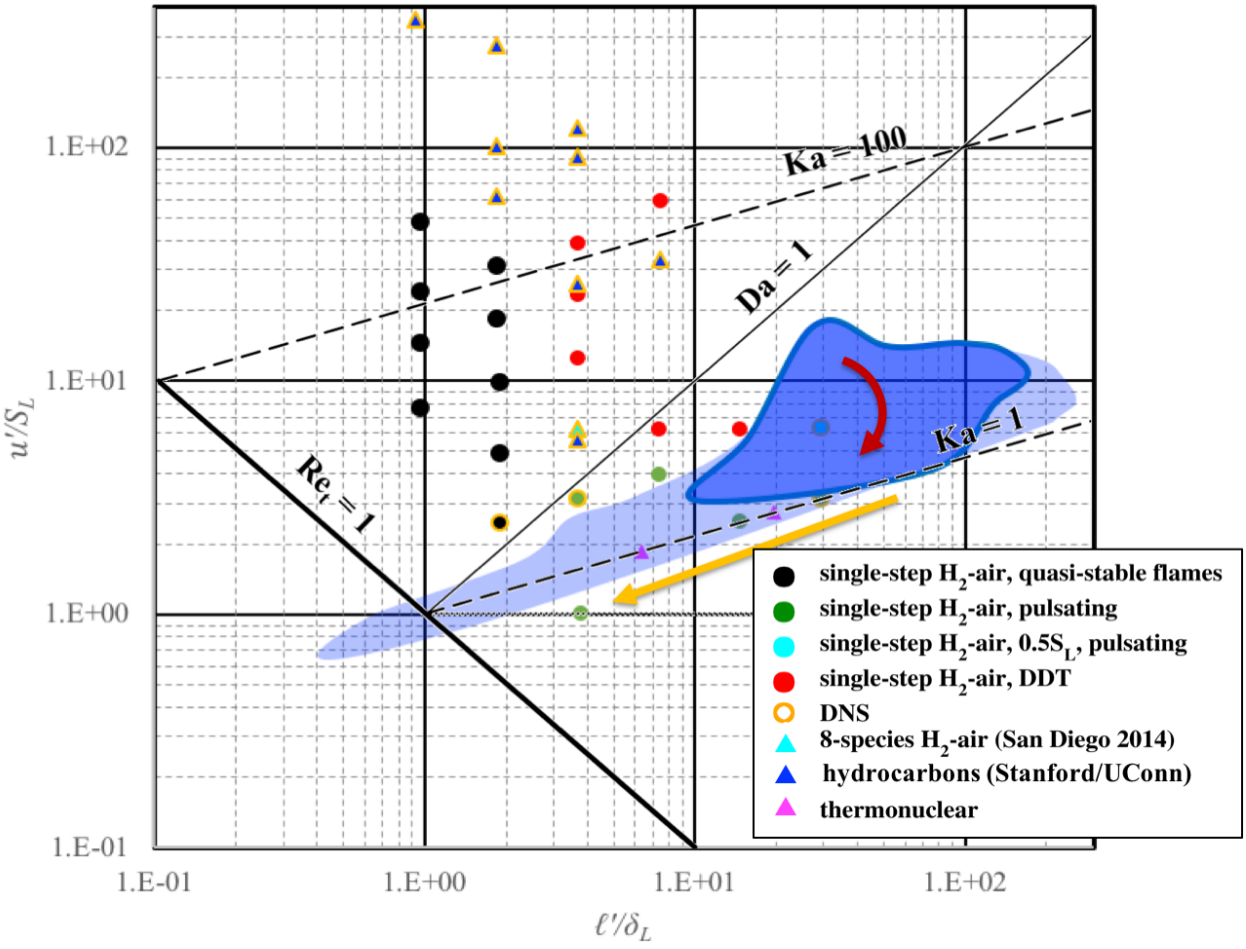

Figure 11 Borghi diagram for NRL and Texas A&M databases of turbulent premixed flames [9, 10, 11, 14, 16, 31, 36], with regime regions obtained in P08h indicated by lighter (all SDs) and darker (flame SDs) blue regions. Black points are the cumulative regimes seen in SD-C. Arrows indicate the general drift of hot (red) and cold (yellow) fluid over the simulation time.

To put this in a broader context, Im [46] discusses state-of-the-art work done in high Re and Ka flows to-date, summarized by the Borghi diagram in Figure 12. Few of the previous studies reviewed simultaneously achieve regimes near the high length and velocity scales as in this DNS. Furthermore, the TST DNS configuration provides a realistic geometric configuration without

external turbulence forcing, which captures unique flow conditions and allows us insight into the "reaction sheet" flow regimes above $Re = 100$.

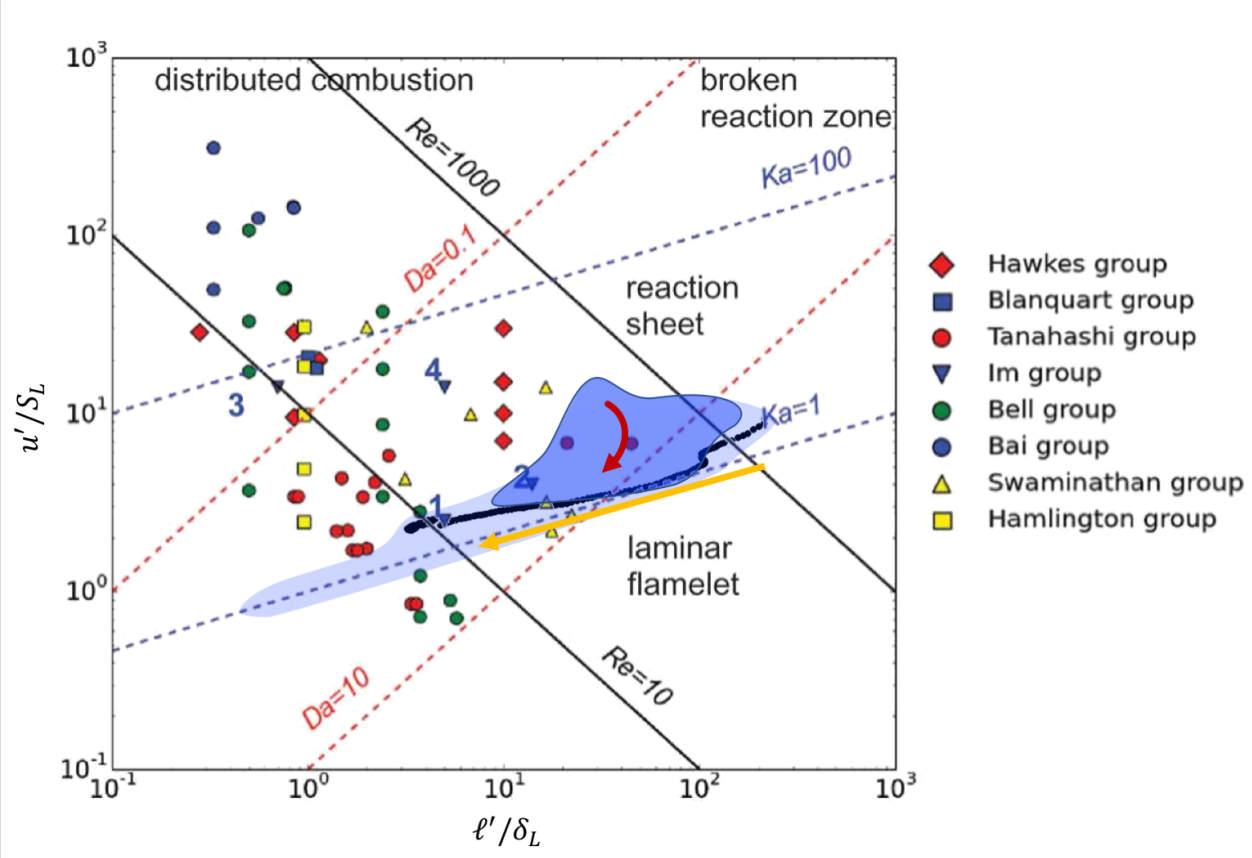

Figure 12 Borghi diagram for turbulent premixed combustion [46] with regime regions obtained in P08h indicated by lighter (all SDs) and darker (flame SDs) blue regions. Black points are the cumulative regimes seen in SD-C. Arrows indicate the general drift of hot (red) and cold (yellow) fluid over the simulation time. Original figure from Direct Numerical Simulations of Statistically Stationary Turbulent Premixed Flames by Im, Arias, Chaudhuri, and Uranakara in Combustion Science and Technology reprinted by permission of Taylor and Francis Ltd, http://www.tandfonline.com.

Mach, Karlovitz, and Taylor Reynolds Numbers

Turbulent Mach number, Karlovitz number, and Taylor Reynolds number are important parameters to quantify the speed, compressibility, and turbulent intensity of the flow. At low Mach numbers, flow can be considered incompressible. However, at larger Mach numbers, such as in the case in realistic propulsion flows, compressibility effects dominate. The turbulent Mach number is based on $\delta U = |\delta u_i|$ and the sound speed, $a = \sqrt{\gamma RT}$

(14) $$M_t = \frac{\delta U}{a}.$$

The Karlovitz number, Ka, is the ratio of the chemical and Kolmogorov timescales. The chemical timescale is a measure of the speed of the reactive processes in the flame and is determined by the evolving laminar flame thickness, δ_L and laminar flame speed, S_L determined by the flow field immediately ahead of the flame front,

(15) $$\tau_c = \frac{\delta_L}{S_L}.$$

The Kolmogorov timescale is related to the smallest scales in the flow and is determined by the kinematic viscosity and the energy dissipation rate,

(16) $$\tau_\eta = \left(\frac{\nu}{\varepsilon}\right)^{\frac{1}{2}}.$$

The Karlovitz number is then, the ratio of (15) and (16),

(17) $$Ka = \frac{\tau_c}{\tau_\eta}.$$

To illustrate the range of turbulent Mach and Karlovitz numbers attained, Figures 13 and 14 show joint probability density functions (JPDFs) for each flame SD-F1 through F5 and the pre-flame compressed region, SD-C. Analysis is performed at 0.4 ms such that the flame and non-reacting SDs are well developed.

As fuel approaches the flame brush, a large portion of the fluid begins to reach M_f up to $0.4 - 0.5$, while a smaller, yet appreciable amount nears 0.75. Simultaneously, Karlovitz numbers reach as high as 400 with extreme excursions above 1000. As the flow progresses through the flame, M_f initially drops upon entering the flame brush from SD-C, then tends to decrease at high Ka, while increasing at low Ka. In the pre-flame compressed SD, distinct "ribs" form along M_f at low Ka. These are indicative of compression waves within SD-C. Figure 14 shows good agreement

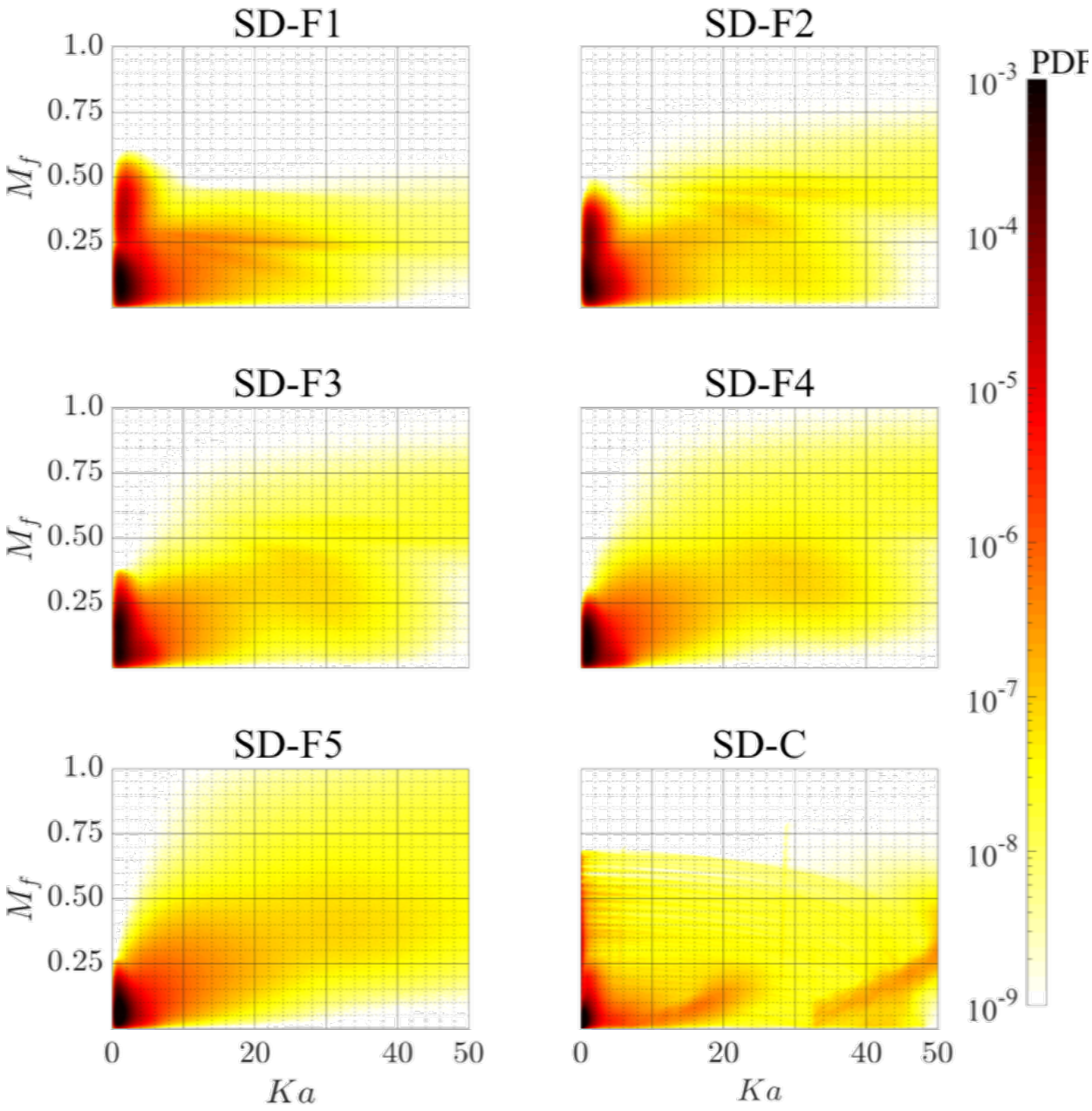

Figure 13 Characterization of turbulent Mach number and Karlovitz number distribution in the flow within and ahead of the flame at 0.4 ms for case P08h.

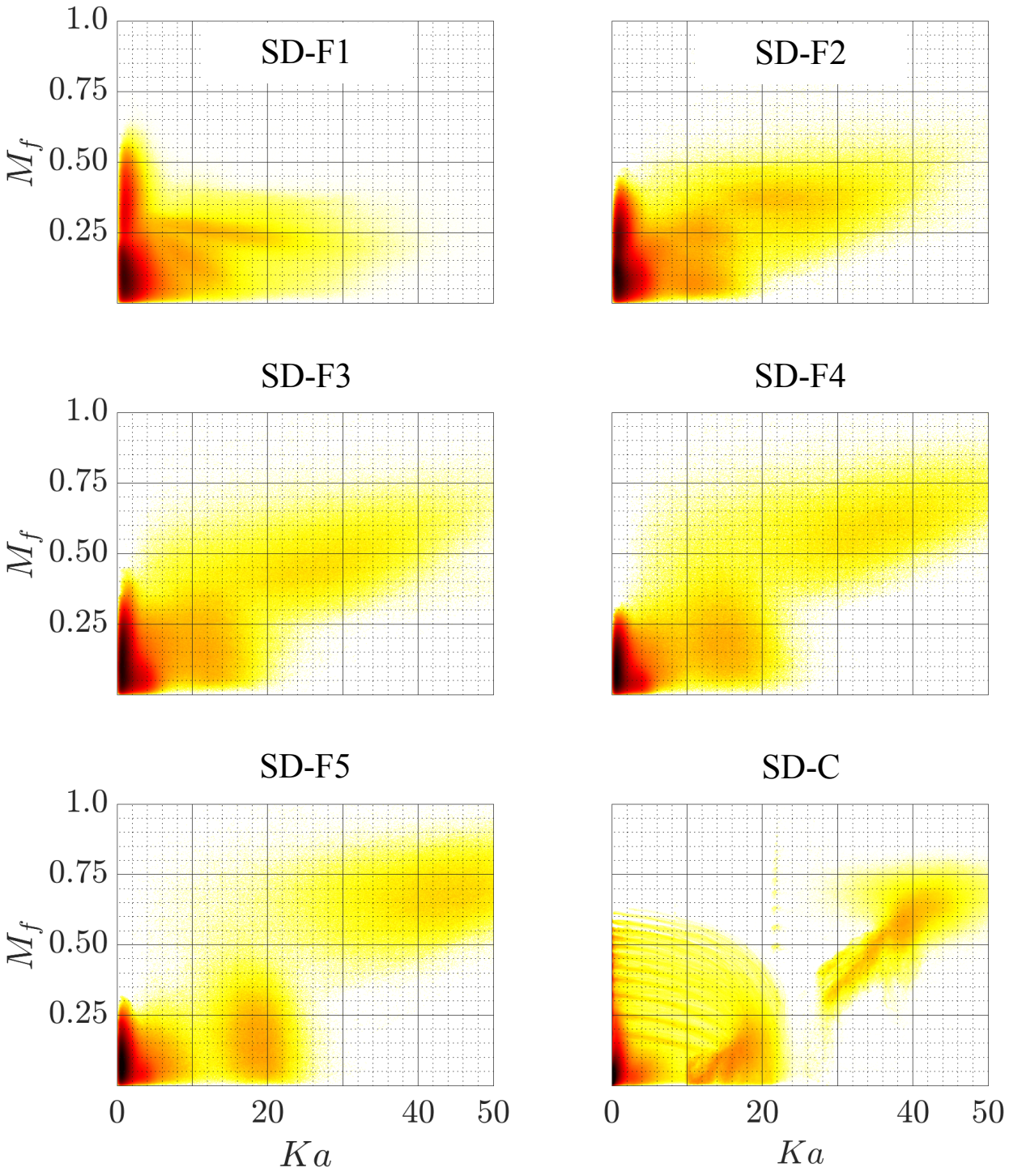

Figure 14 Characterization of turbulent Mach number and Karlovitz number distribution in the flow within and ahead of the flame at 0.4 ms for case P08. Colormap is as shown in Figure 13.

with these trends in the lower resolution P08 simulation, with lower probabilities of high M_f and Ka within the flow.

The Taylor-scale Reynolds number, Re_λ, determines a Reynolds number based on the longitudinal Taylor microscale, λ, the length scale used to describe turbulence [39].

$$\lambda = u' \sqrt{\frac{15\nu}{\varepsilon}}, \tag{18}$$

$$Re_\lambda = \frac{u'\lambda}{\nu}. \tag{19}$$

Using a similar rationale as for the integral length scale, we are interested only in the SD volume averages of the Taylor microscale and Taylor Reynolds numbers. Therefore, we can substitute volume averaged quantities into (18),

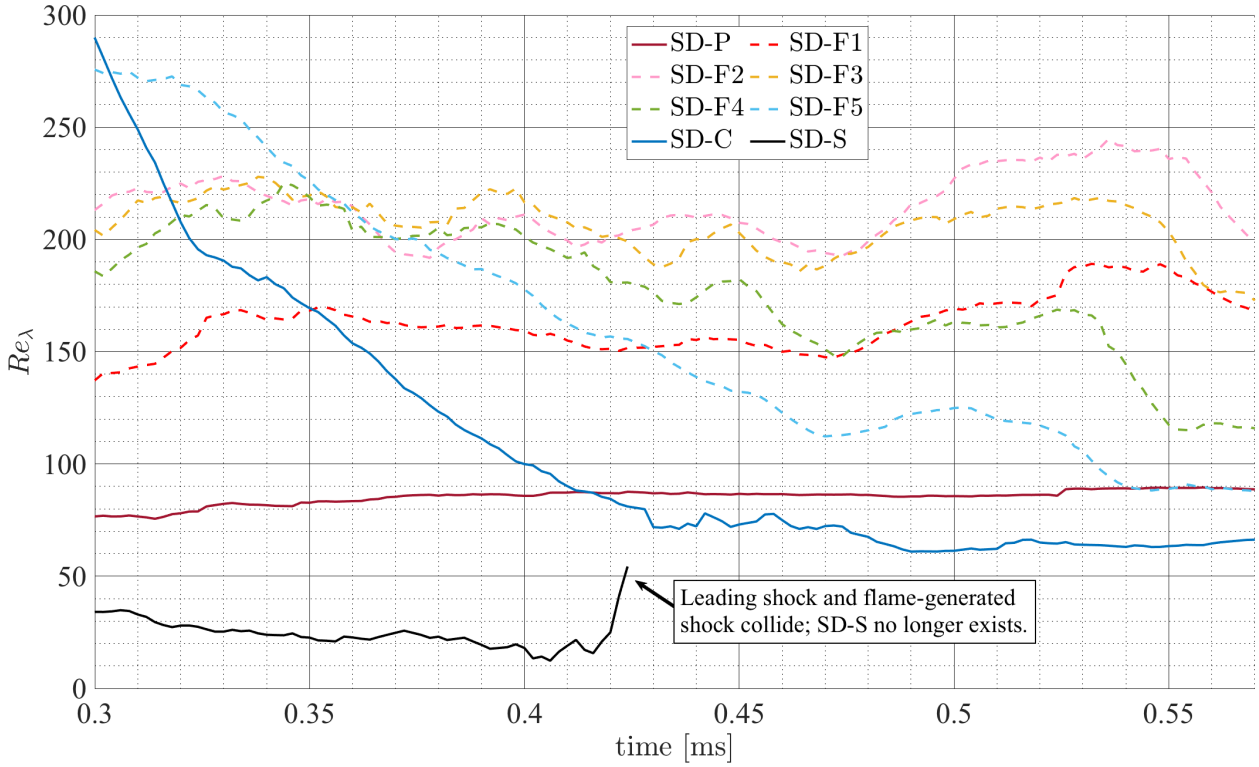

$$\langle\lambda\rangle_V = \langle u'\rangle_V \sqrt{\frac{15\langle\nu\rangle_V}{\langle\varepsilon\rangle_V}}, \tag{20}$$

then use (13) and (20) to calculate the Taylor Reynolds number as,

$$\langle Re_\lambda \rangle_V = \frac{\langle u\prime \rangle_V \langle \lambda \rangle_V}{\langle \nu \rangle_V}. \tag{21}$$

The Taylor Reynolds number defined in equation (21) can be considered a measure of turbulence within the flow. Figure 15 shows the evolution of Re_λ over the simulation time. With the exception of SD-S, colder fluid enters the quasi-steady burning period at higher Re_λ than hotter fluid. SD-S exhibits relatively low turbulent intensity over the course of its evolution, as this is fuel that has only been processed by the leading normal shock. This evolution is consistent with the δv components shown in Figure 5 which show low δv in the flow until SD-C. As the flow evolves over the simulation time, SD-S disappears as the leading and flame-generated shocks collide. The trend of Re_λ for most SDs is to decrease over time. This is most prominent in the colder SD-C and the front of the flame brush. Toward the back of the flame brush and in SD-P the

Figure 15 Taylor Reynolds number evolution over quasi-steady simulation time in all SDs for case P08h.

evolution stays relatively constant with the hotter SD-F1 and SD-P showing a slight increase.

Flow Analysis

Many of the same flow dynamics seen in the transverse averages of Chapter V, Figure 5 can be seen in two-dimensional detail in Figures 16 and 17, which show midsection cuts along the x-normal plane of the domain. The pressure (a) shows the pre-flame compressed region, initially thin with high pressure, gradually widen and decrease slightly in pressure as the flame-generated shock approaches and overtakes the leading shock. The rarefaction wave, formed after the flame-generated and leading shocks collide, is most visible in the later frames of the synthetic schlieren (b) and temperature (c). A contact surface between the incoming flow from the injection plate and

the displaced flow from the shock system ahead is most notable in temperature (c) between 5 and 10 cm. The increase in turbulent intensity across the flame is clearly seen from (d) and (e), as the transverse velocity components are approximately equivalent to the fluctuating velocity components, while the axial velocity (f) provides important bulk flow speed data which will be discussed in Chapter VII. Many of the panels also show the previously discussed compression waves in SD-C and SD-S.

While P08, shown at 0.4 ms in Figure 17, exhibits very similar behavior, prior to the shock collision, P08h displays higher pressures toward the front of SD-C. After the flame-generated and leading shocks collide, P08 maintains higher peak pressures in the new, combined SD-C/S.

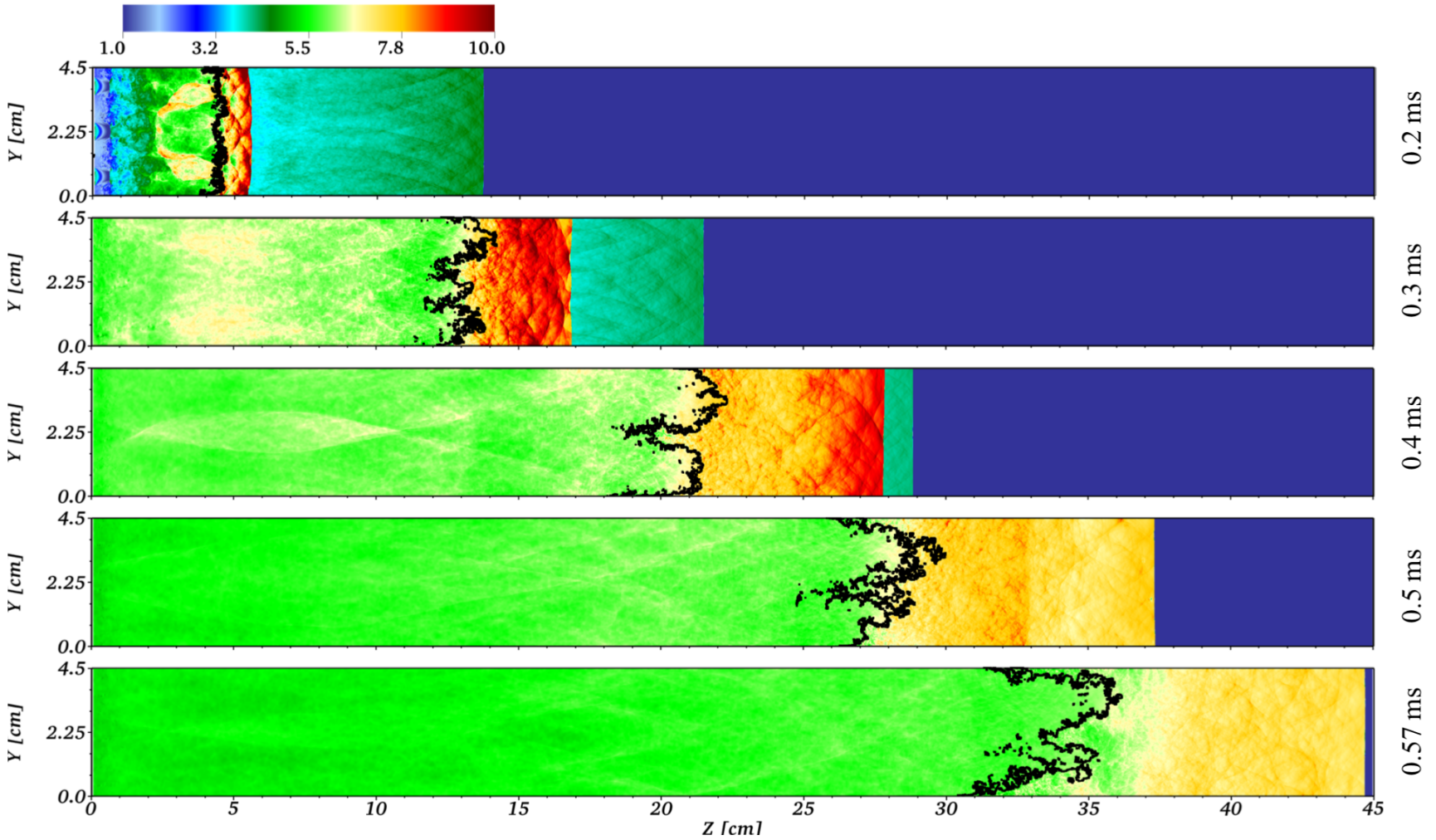

Figure 16 (a) Two-dimensional midsection cuts of (a) pressure [atm], (b) synthetic schlieren, (c) temperature [K], and (d-f) velocity components [m/s] with the flame brush overlaid as a solid black line at 0.2, 0.3, 0.4, and 0.5, and 0.57 ms for case P08h.

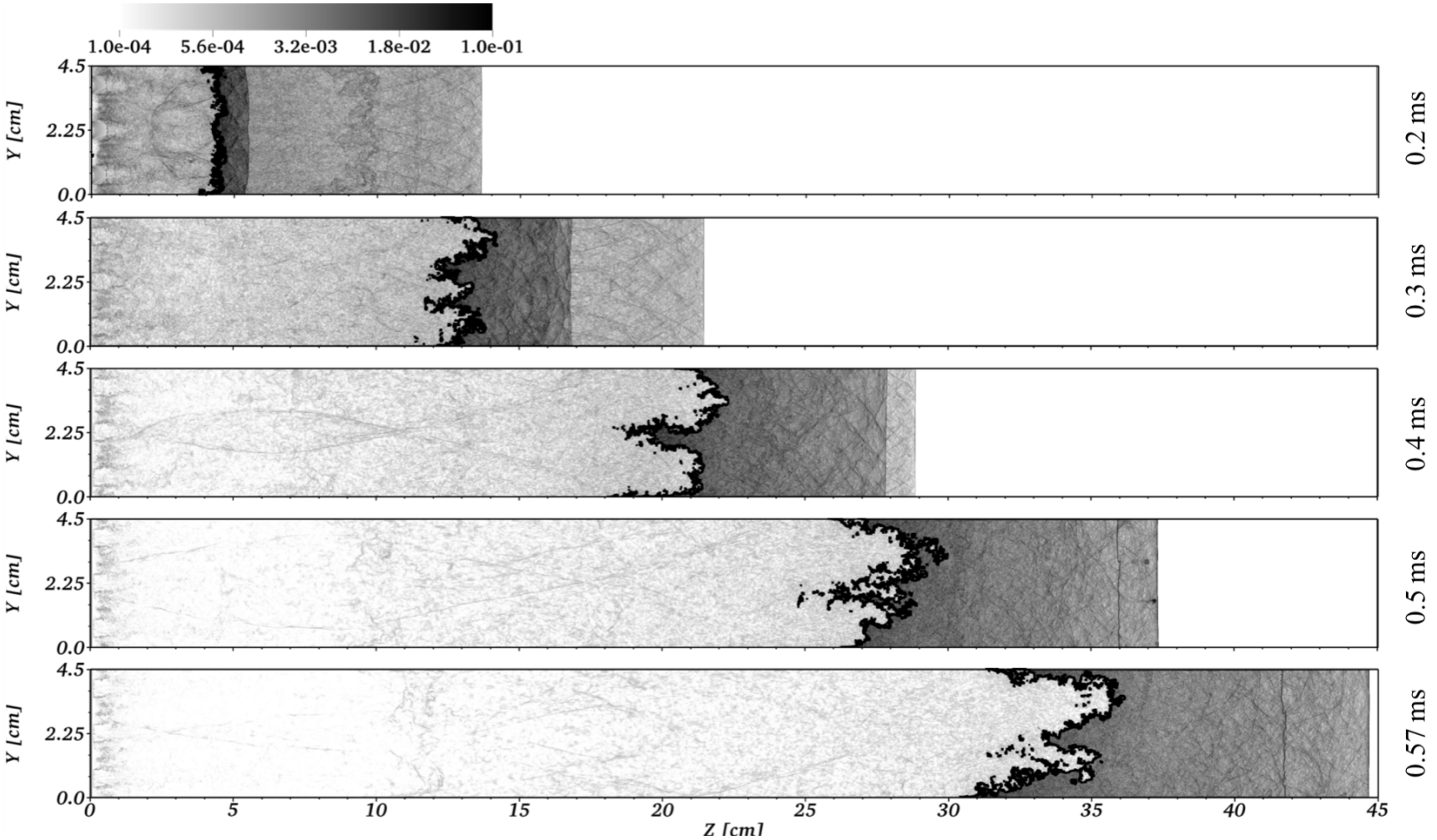

Figure 16 (b) Continued.

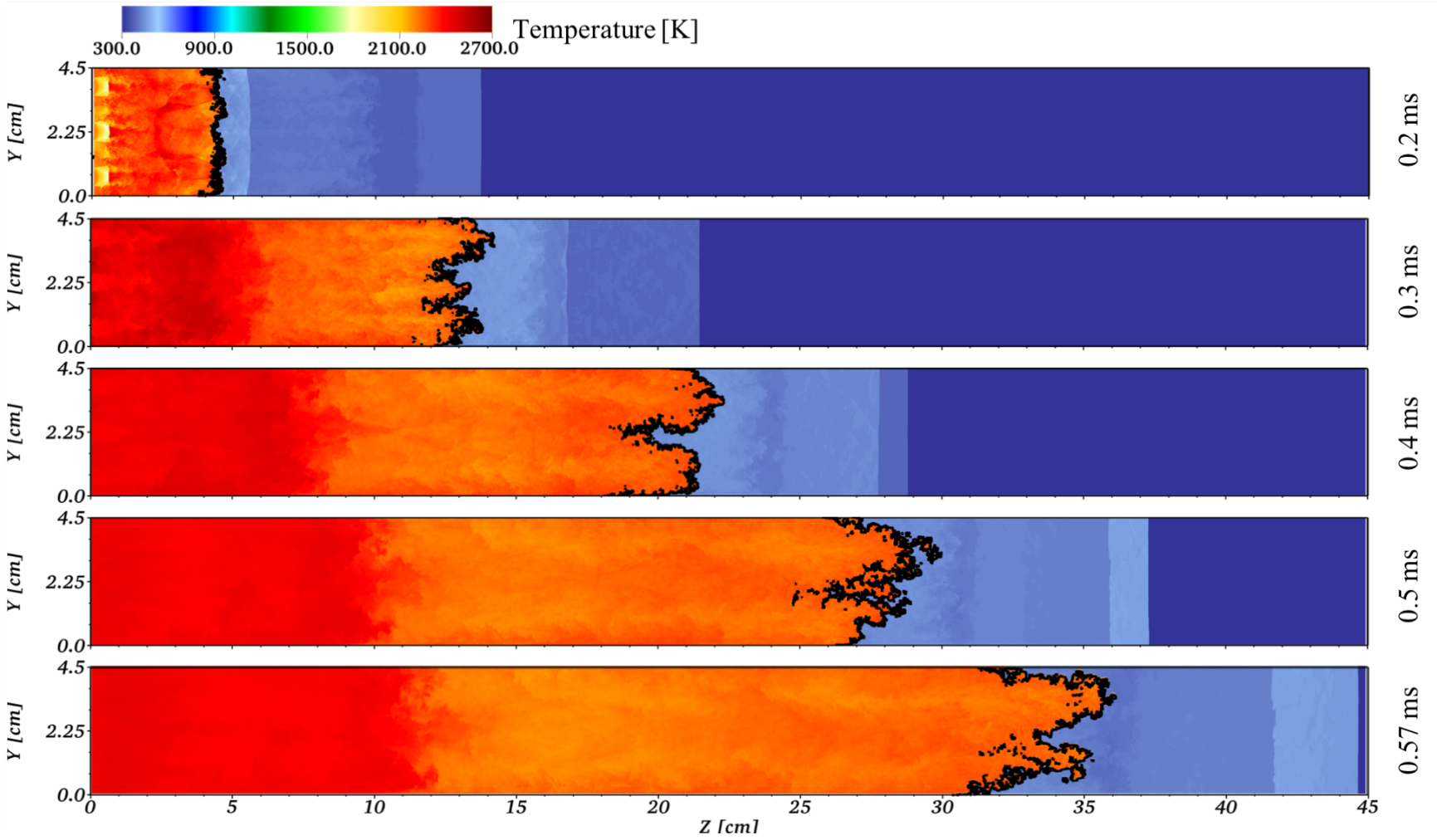

Figure 16 (c) Continued.

Figure 16 (d) Continued.

Figure 16 (e) Continued.

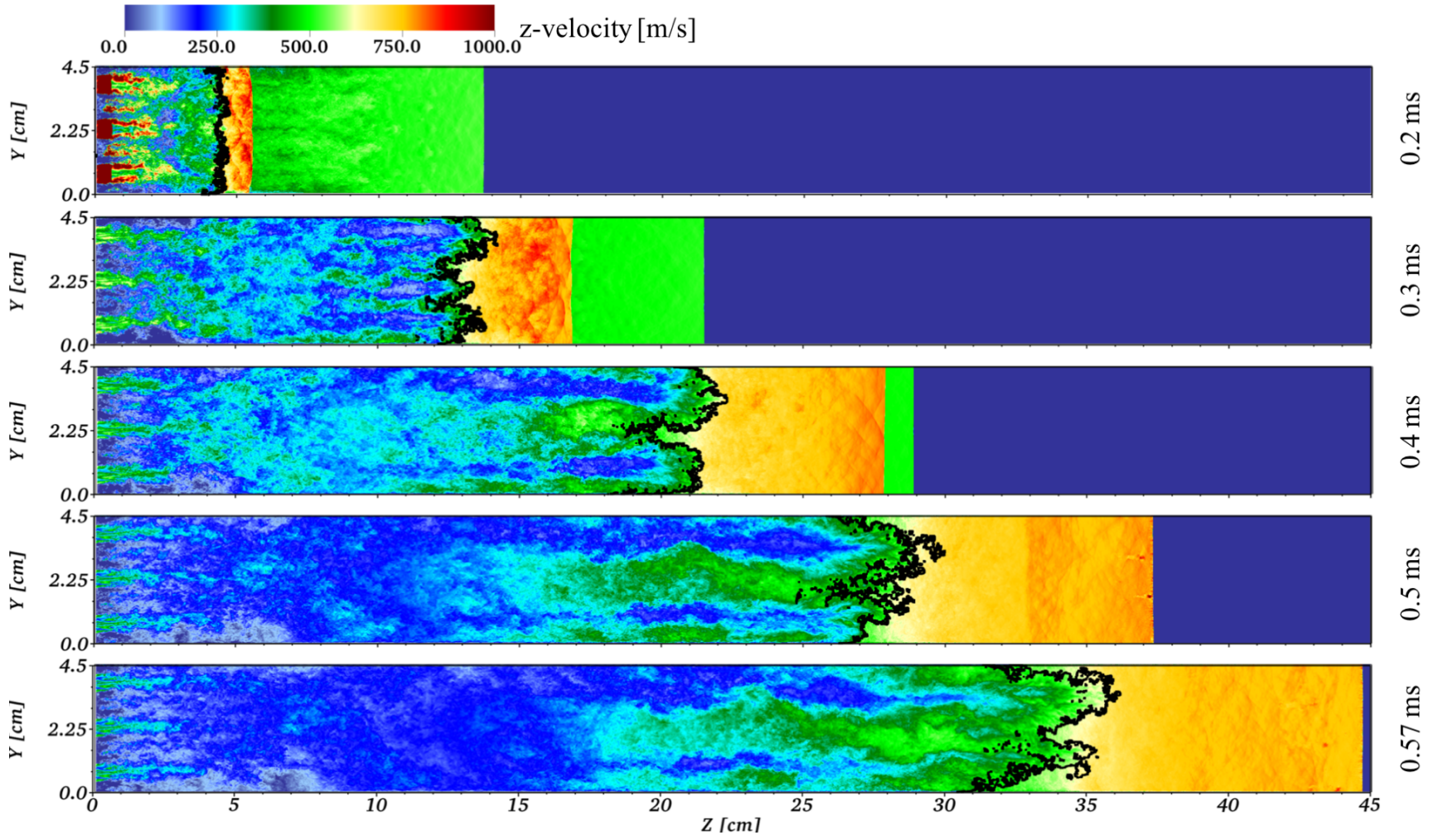

Figure 16 (f) Continued.

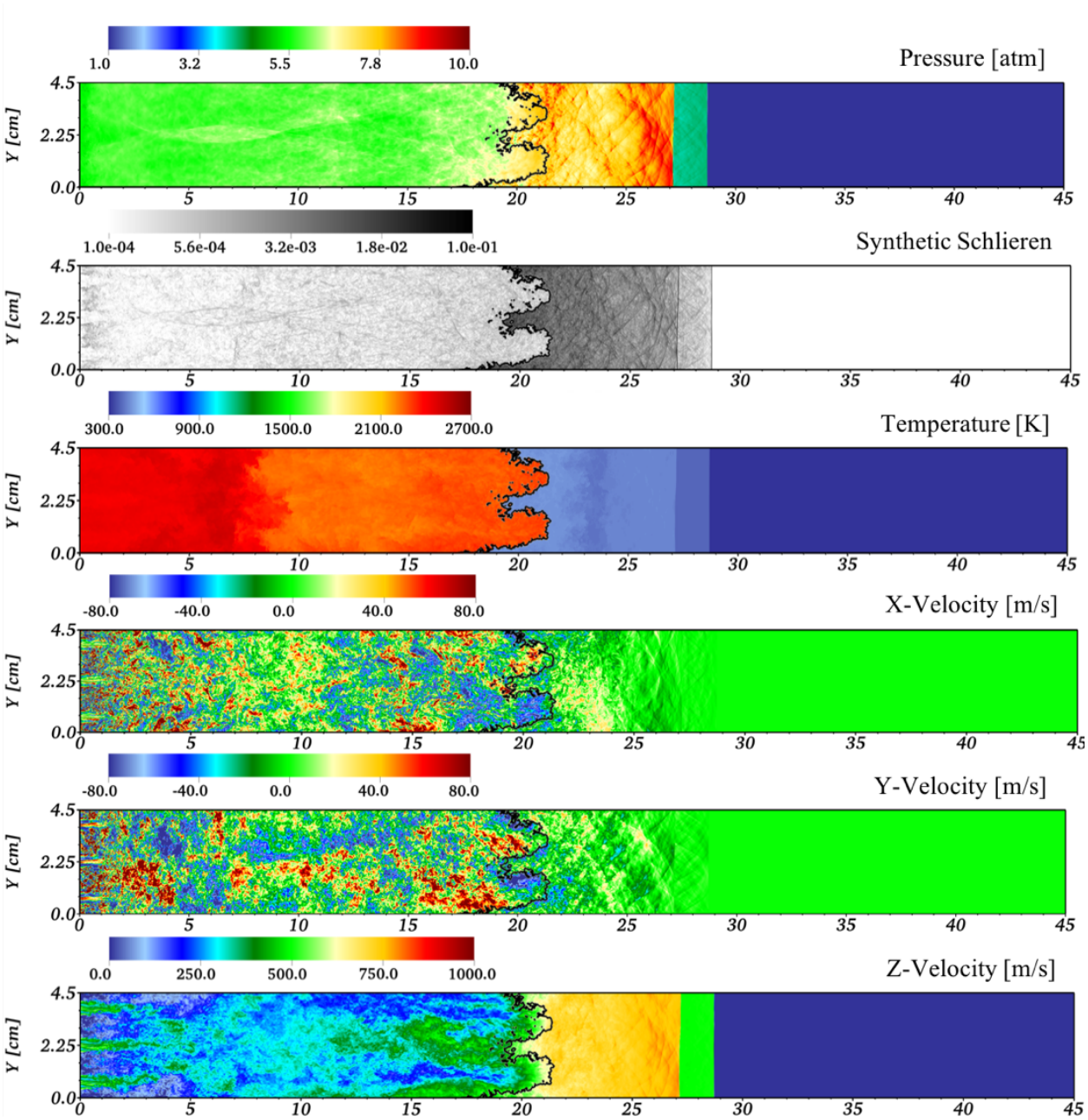

Figure 17 Two-dimensional midsection cuts of pressure, synthetic schlieren, temperature, and velocity components with the flame brush overlaid as a solid black line, at 0.4 ms for case P08.

Probability Densities

Probability density functions (PDFs) through the flow SDs are shown in Figures 18 and 19 for both DNS. Pressure, temperature, and density are multi-modal due to the PDF sample distribution coverage of fuel, flame, and product regions. Transverse and fluctuating velocity components are predominantly isotropic, however there appear to be a large-scale swirling motions behind the flame visible in the transverse velocity components shown in Figures 16 (d-e) and Figure 17. SD-C shows supersonic flow ahead of the flame brush, while fluctuating Mach numbers are highest toward the product side of the flame and, to a lesser extent, within the SD-P itself. Compression waves in SD-S and SD-C cause the apparent "oscillations" in fluctuating Mach number and δv_z. Local flow Reynolds number, based on the domain width, is largest within the flame brush and SD-C.

In P08, Karlovtitz number extents exhibit an overall increase, from near 20 in the post-shock flow, up to several hundred in the product region. Average Karlovitz numbers within and behind the flame brush range from 10 to 20, while fuel regions average lower. The higher resolution P08h case shows similar trends with the exception of Ka in the flame brush, which is more in line with that of SD-P than in the lower resolution simulation. In P08, energy dissipation rate also increases as the flow passes through the flame brush, from reactants to products. While enstrophy shows a similar trend to ε, SD-C also produces small quantities of high enstrophy. P08h follows the same general trends as P08, with moderately larger ε in most SDs and substantially larger Ω in all SDs.

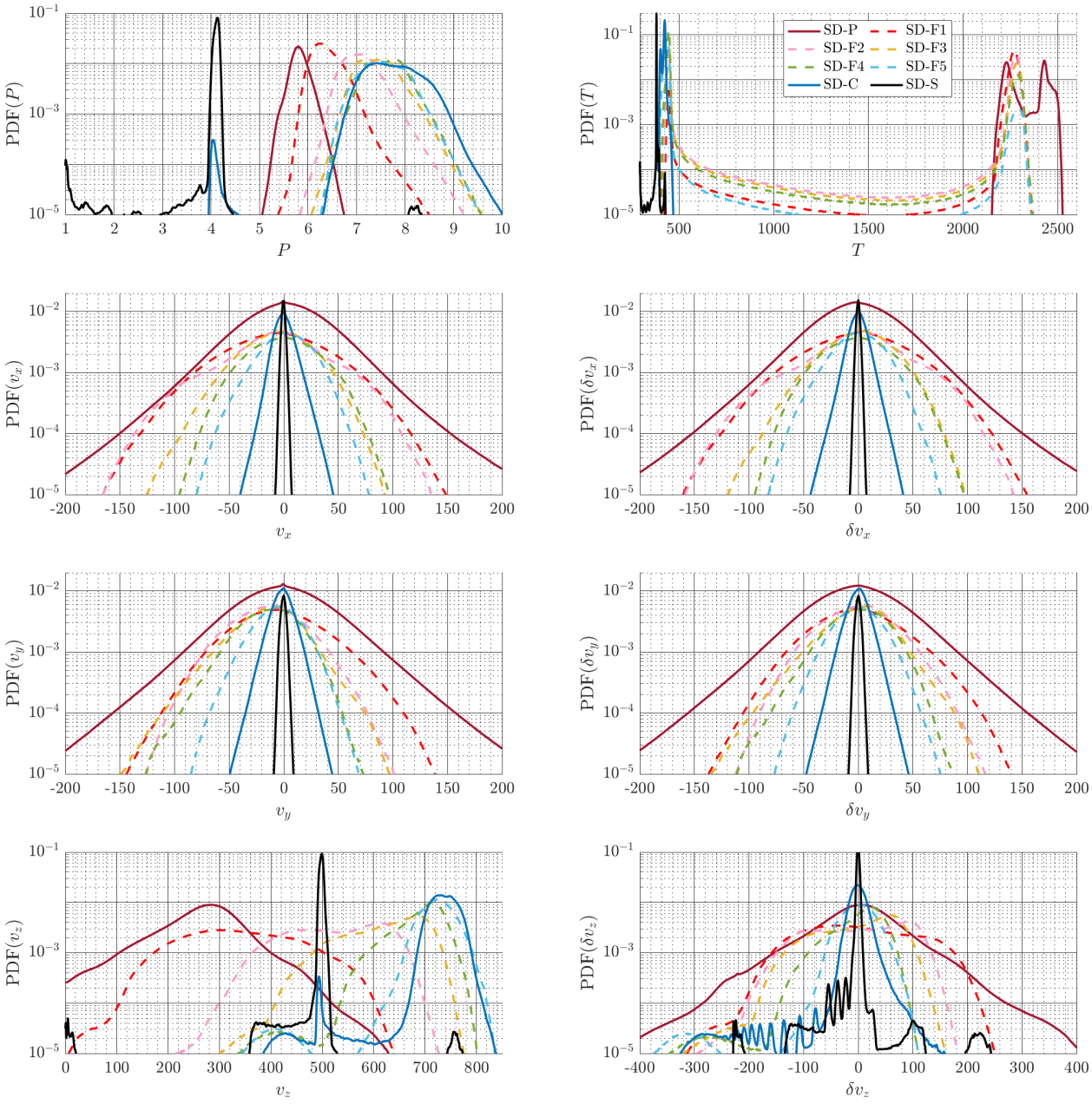

Figure 18 Probability density functions across all SDs for thermodynamic, velocity, and turbulence characterization properties at 0.4 ms in Case P08.

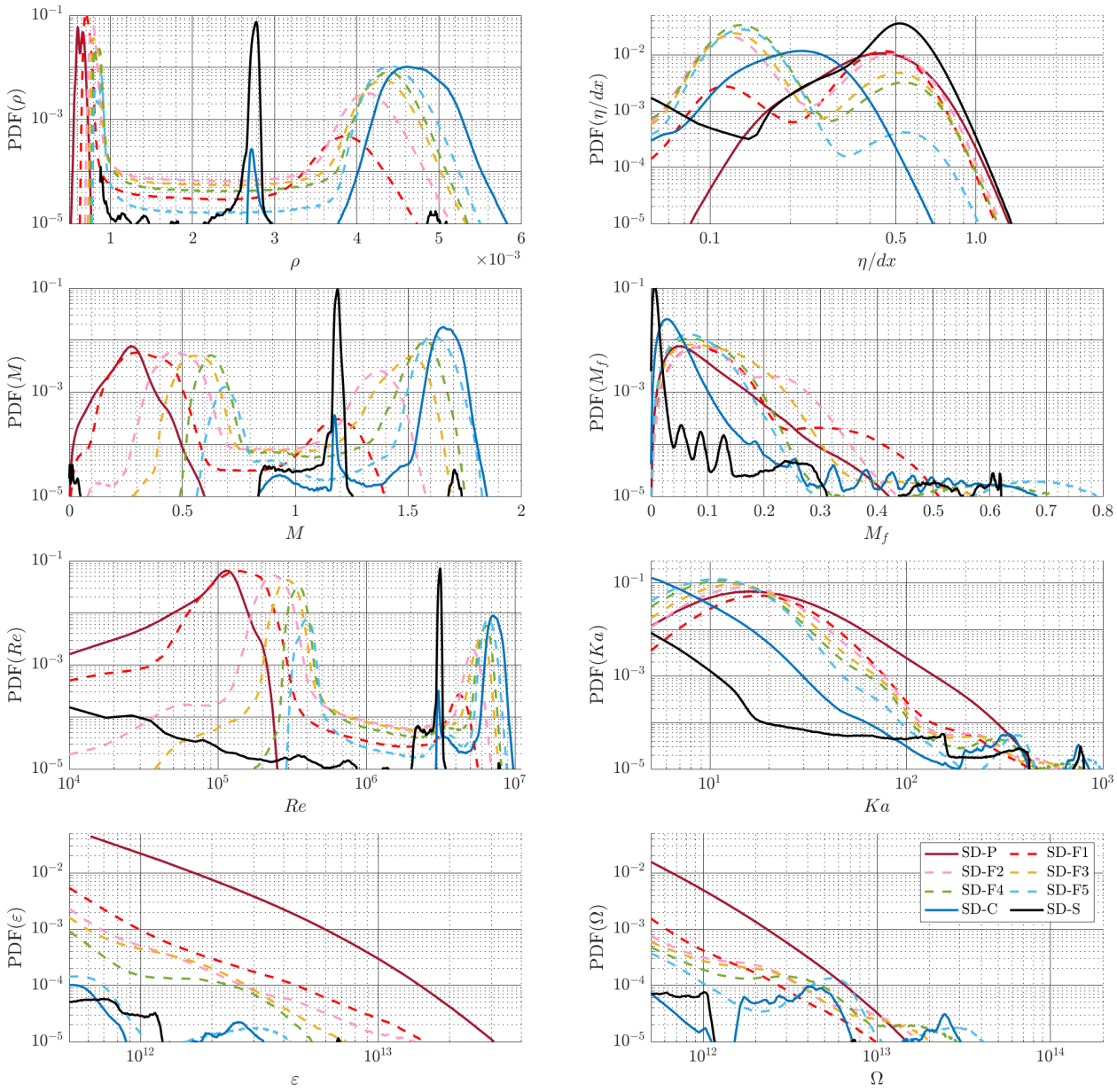

Figure 18 Continued.

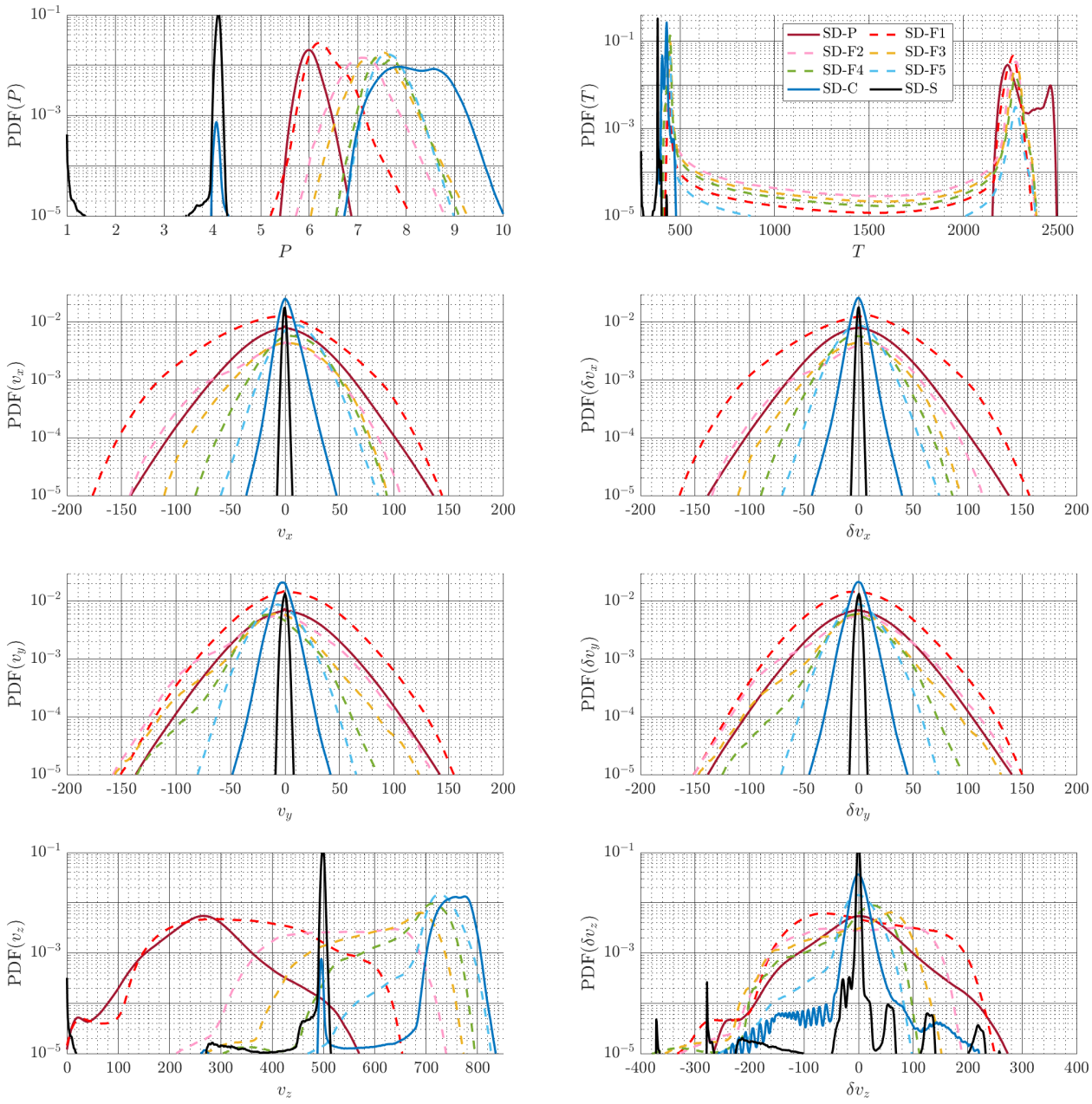

Figure 19 Probability density functions across all SDs for thermodynamic, velocity, and turbulence characterization properties at 0.4 ms in Case P08h.

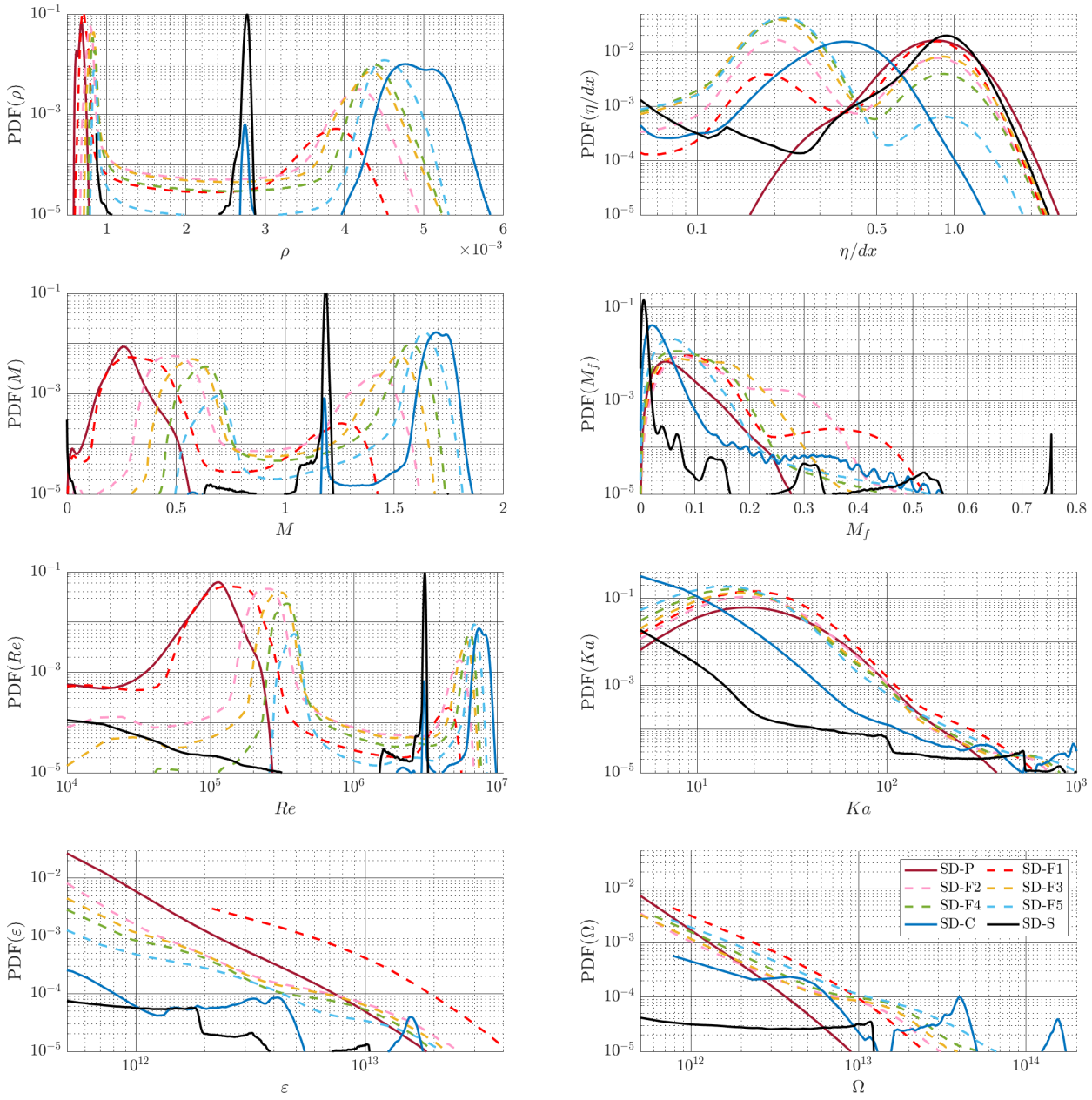

Figure 19 Continued.

Kolmogorov scale, normalized by cell size, is used to infer the degree to which the smallest scales of flow are resolved by the computational grid. Rather than a single value for the domain, however, the highly unsteady spatial and temporal nature of the flow field considered requires evaluation of local viscosity and dissipation rates, which are then considered within their respective subdomains. While this unsteady nature brings into question the applicability of Kolmogorov type turbulence to this flow, $\eta = (\nu^3/\varepsilon)^{1/4}$ provides a length scale based on the energy dissipation and viscosity, which does indeed indicate the small, dissipative length scales which will allow us to assess full-scale flow resolution. This Kolmogorov scale resolution, although debatably borderline for DNS, shows that a substantial amount of the flow field resolves η with half a cell width in P08 and close to a full cell width in P08h.

CHAPTER VII

FLAME SPEED

Flame speed is an essential parameter for the development of turbulent combustion models and, ultimately, accurate prediction of a combustion engine's performance. Therefore, turbulent flame speed is one of the focal points of combustion research. This speed is defined by the consumption rate of reactants, i.e. the volume of incoming flow per unit area of the mean flame front. For low intensity, large scale domains, this is also equal to the propagation speed of the flame front. However, this equivalence is questionable for flames within supersonic flows and in the extreme regimes presented in this configuration.

Flame Burning Speed

Turbulent flame burning speed, S_T, can be numerically calculated as the burning rate of the flame through an incoming turbulent flow,

$$S_T = \frac{\dot{m}}{L^2 \rho}, \tag{22}$$

where $\dot{m}$ is the total fuel consumption rate in the domain, L^2 is the domain cross sectional area, and ρ is the incoming fluid density. The choice of this density affects the resulting S_T and defines the reference frame for the calculated speed. To determine S_T in the reference frame of the bulk flow speed approaching flame, we use the transverse averaged density in the plane immediately ahead of the flame front. It can be assumed from mass conservation that all flow that the flame passes through is burned and converted to products.

Flame Displacement Speed

In some cases, as in experimental settings, S_T cannot be determined directly and the flame displacement speed, S_D, is often used in its place. S_D, is a physical displacement speed calculated as a finite difference of flame front location with respect to the bulk flow speed ahead:

(23) $$v_f = \frac{z_{f,t_2} - z_{f,t_1}}{t_2 - t_1},$$

(24) $$S_D = v_f - u_F.$$

Here, v_f is the flame front speed in a stationary reference frame, $z_{f,t}$ is the flame front location at some time, t, and u_F is the bulk flow speed in the plane directly ahead of the flame front.

These components are illustrated in Figure 20 where two representative flame instances are shown at z_{f,t_1} and z_{f,t_2}. A shock precedes the flame position. The bulk speed location can be chosen such that it is exactly the flow velocity that the flame "sees" ahead of it, i.e. in the transverse plane immediately preceding the flame front. The finite difference in (23) is taken over a time step equivalent to 100kHz, around the current limitation of experimental measurement capabilities, although still a higher resolution than the flame speeds measured with PIV and chemiluminescence in the experimental TST facility.

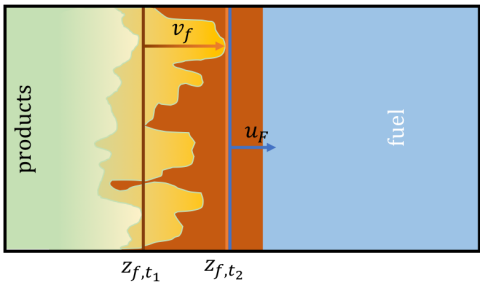

Figure 20 Flame displacement speed.

Figure 21 shows how a synthetic S_D given by (24) compares to the turbulent burning speed based on the rate of fuel consumption as in (22) for the numerical TST. Also shown are the same flame speed comparisons performed on several flame in the box configurations [9-12, 19, 31, 36] (simulations were performed with H_2-air fuel where not otherwise specified). In all cases, the two flame speed measurement methods loosely follow the correlation line shown in black, but can differ significantly.

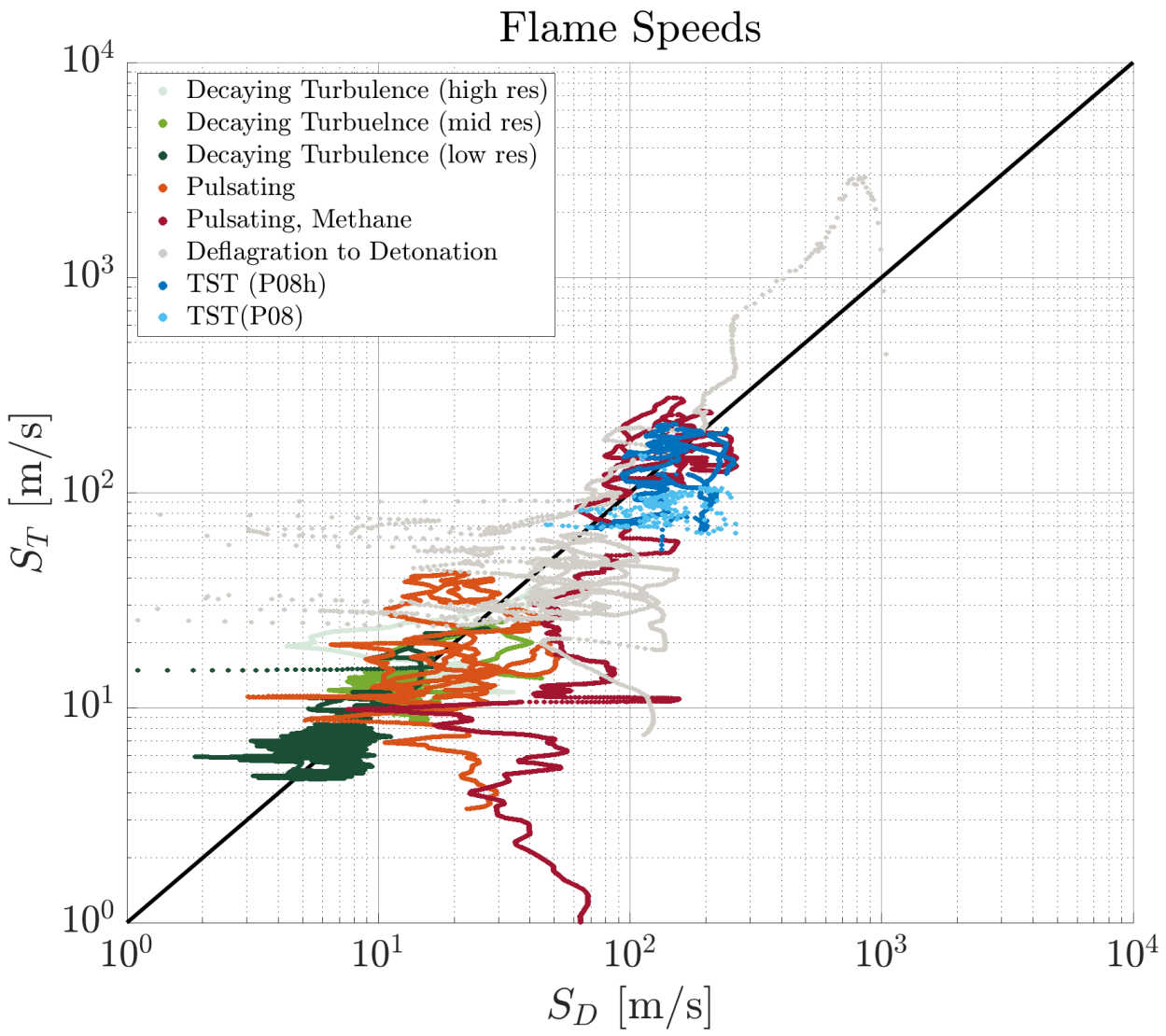

Figure 21 Flame burning speed and flame displacement speed correlation for several turbulent flame studies.

For steady-state or low turbulent intensity flames, S_T and S_D can generally be used interchangeably. However, as shown in Figure 22, at the high speed, highly compressible, and highly turbulent regimes encountered in this TST configuration, the differences between the two speed measurements can be substantial. Experimental flame speed measurement methodology averages the bulk flow speed over some volume ahead of the flame, $z_{f,t} + \delta z$, usually including the majority of the compressed region. The resulting flame displacement speed garnered by experimental-type averaging over a volume of SD-C or only averaging the plane ahead of the

flame fall within the blue region in Figure 22. The variability in the definition of u_F affects S_D by up to 40 m/s, while S_D and S_T themselves can differ by $50 - 80$ m/s. This accounts to flame speed differences of up to 50%. Furthermore, these discrepancies are expected to increase at higher turbulent intensities, closer to DDT. [47]

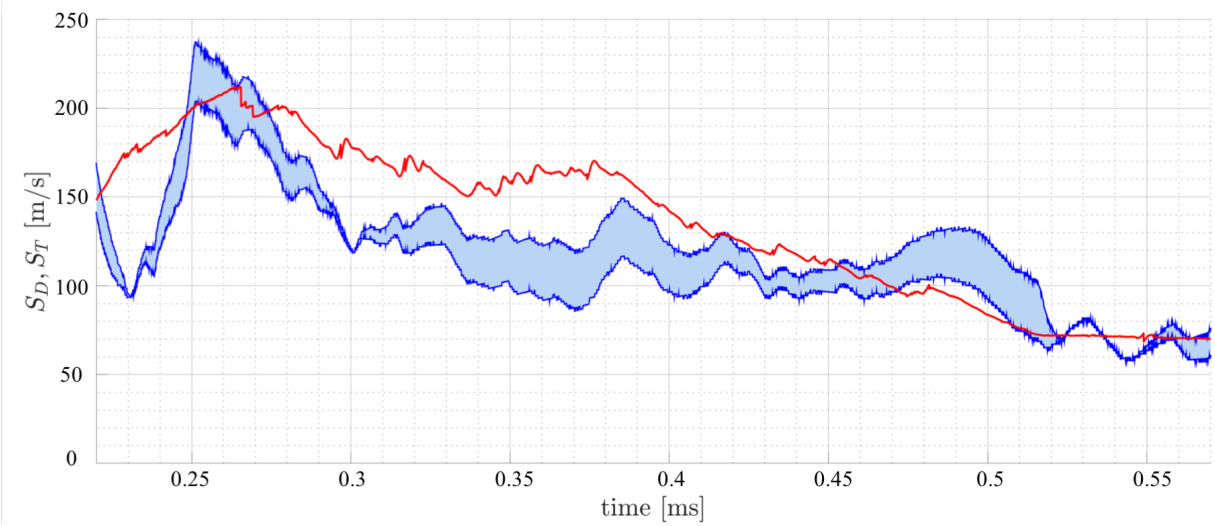

Figure 22 Flame burning (red line) and displacement (blue region) speed during a period of quasi-steady burning rate for Case P08h.

Turbulent flame speeds, which range from $\sim 75 - 175$ m/s during the period of quasi-steady burning after 0.3 ms, are roughly proportional to the turbulent velocity fluctuations, and are consistent with those shown in Figures 5, 16, and 17. The nature and source of this turbulence were introduced in Chapter V and will be explored further in Chapter VIII.

CHAPTER VIII

TURBULENCE GENERATION

To study the fundamental nature of the turbulence, particularly flame generated turbulence, we consider the enstrophy budget in in the flame region:

$$\frac{\mathrm{D}\Omega}{\mathrm{Dt}} = \omega_i \omega_j S_{ij} - \omega_i \omega_i S_{kk} + \omega_i \frac{\varepsilon_{ijk}}{\rho^2} \frac{\partial \rho}{\partial x_j} \frac{\partial P}{\partial x_k} + \omega_i \varepsilon_{ijk} \frac{\partial}{\partial x_j} \left(\frac{1}{\rho} \frac{\partial \tau_{km}}{\partial x_m} \right). \tag{25}$$

Enstrophy, Ω, is the magnitude of vorticity squared and can be interpreted as a measure of the kinetic energy of a fluid as a result of turbulence. On the right-hand side (RHS) of the above equation there are several terms with distinct effects on the dynamics of turbulent flows. The first term on the RHS governs vortex stretching, arguably the most important mechanism in turbulence dynamics. Vortex stretching represents, the creation of vorticity. This is the mechanism which transports turbulent energy to smaller scales. The second term on the RHS is the dilatation. It captures the effects of the expansion due to heat released in combustion as well as the compression largely seen in the region between the flame and the leading shock. The third term on the RHS is the baroclinic torque. This accounts for the generation of turbulence due to misalignment of density and pressure gradients. Finally, the last term on the RHS is viscous dissipation, which describes how turbulence diffuses due to dissipation [45].

Figure 23 shows the time evolution of the enstrophy budget components within the flame brush for both DNS cases. While vortex stretching and dilatation are both present in reacting and non-reacting flows, baroclinic torque is contributed mainly by the flame, and is dominant in this flame brush enstrophy budget. Dilatation is also significant, as it is enhanced by the exothermic reactions within the flame. Viscous dissipation present, but is generally the smallest contributor to the budget. Both DNS cases exhibit similar trends but differ appreciably in magnitude. The higher resolution run reported larger values of all components. Vortex stretching, dilatation, and

baroclinic torque roughly doubled, while viscous dissipation experienced a much larger change, becoming comparable in magnitude to dilatation.

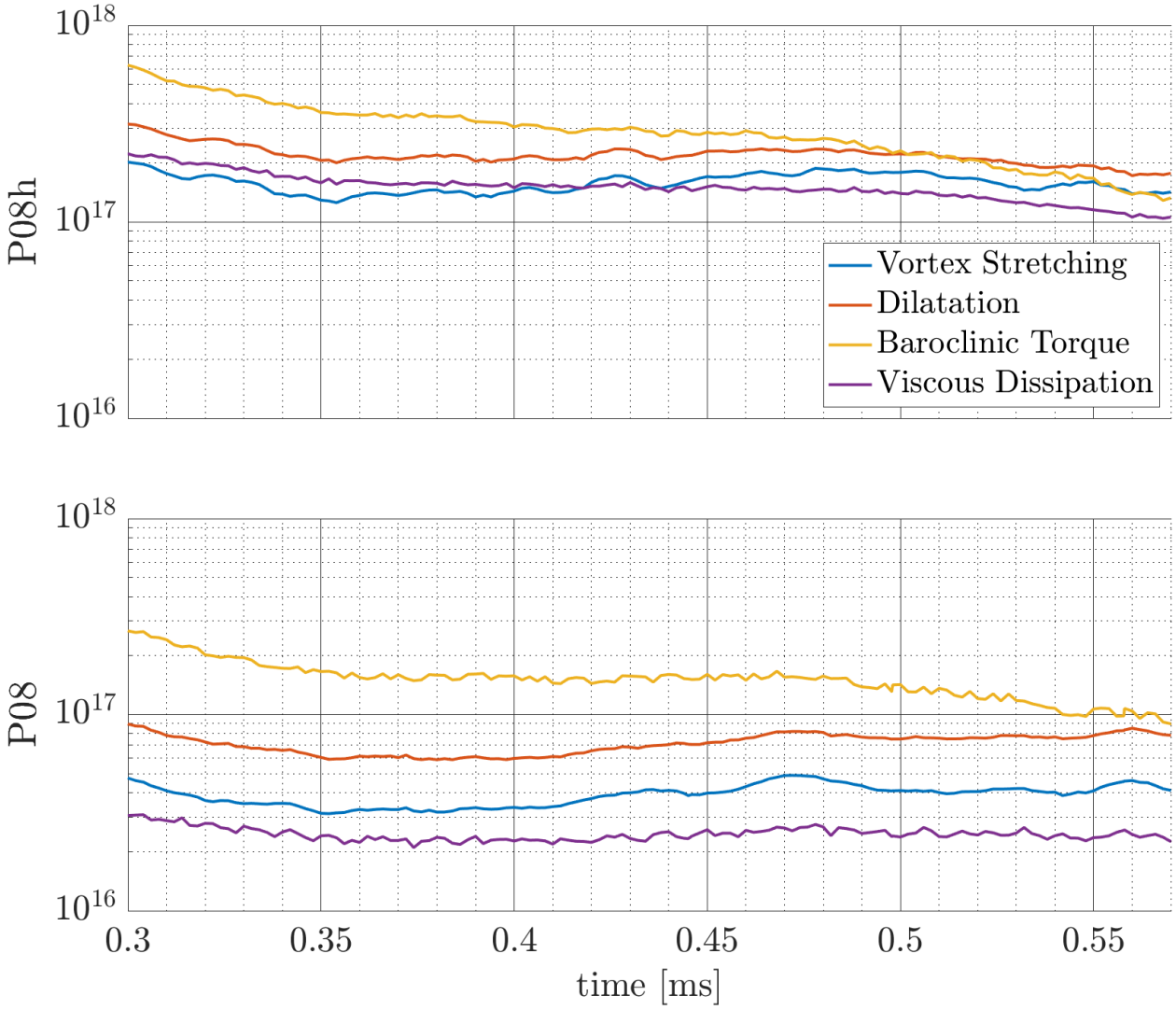

Figure 23 Time evolution for absolute values of enstrophy budget components within the flame.

For a full domain view, Figure 24 shows the flow field of enstrophy magnitude in both DNS after the component values have settled while Figures 25 shows the enstrophy budget components of vortex stretching, dilatation, and baroclinic torque for the same instant (0.4 ms) for case P08h. Consistent with analysis from Chapter VI, turbulence, indicated by enstrophy magnitude, is significant immediately following the inlet jets, dissipates somewhat, and then

increases in the products closer to the flame brush. Figures 24 and 25 show that enstrophy and the enstrophy budget components begin to become significant starting from the right in SD-C, just ahead of the flame. After the moderate increase through SD-C, vortex stretching and dilatation experience a further gain through the flame brush and into SD-P. Baroclinic torque, however, is dominant only within the flame brush itself. This is due to the combination of sharp density gradients and a nearly isobaric flame, which were seen in Chapter VI, Figures 16a and 17.

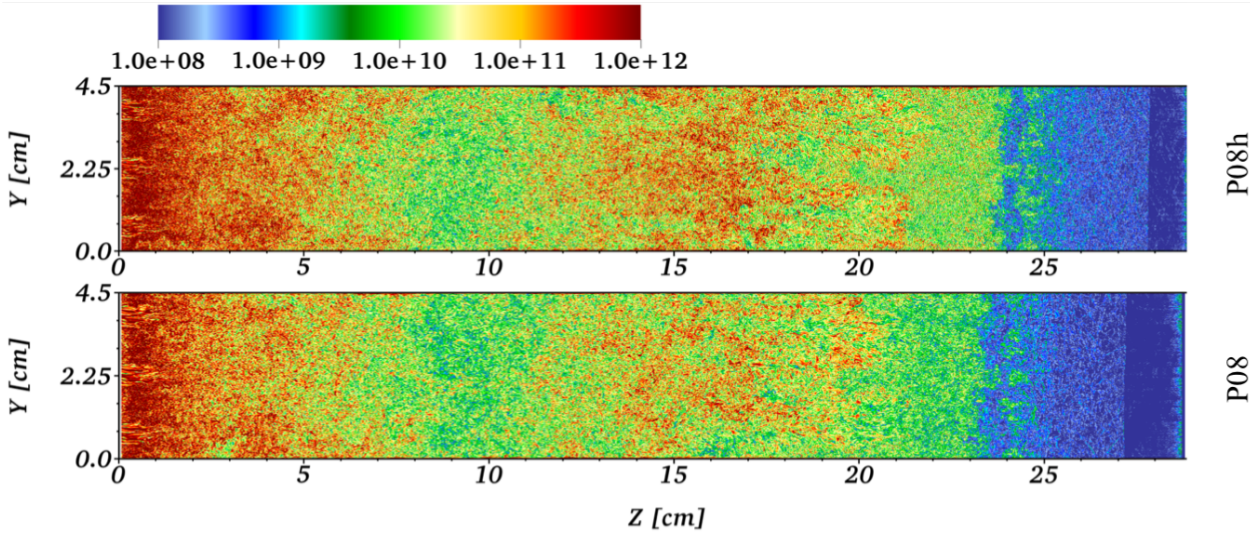

Figure 24 Enstrophy magnitude at 0.4 ms for cases P08h (top) and P08 (bottom).

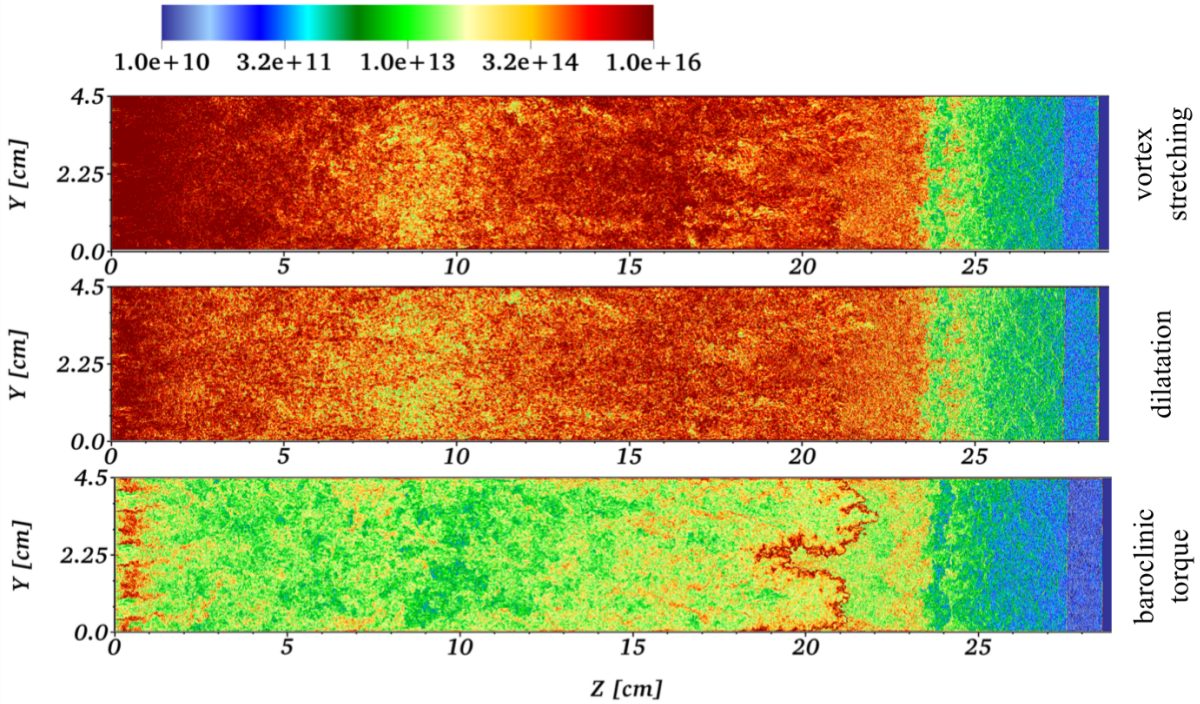

Figure 25 Vortex stretching, dilatation, and baroclinic torque at 0.4 ms for case P08h.

CHAPTER IX

CONCLUSIONS

The work in this thesis has analyzed two large-scale DNS representative of a realistic, unsteady flow configuration in order to determine the flow regimes, flame dynamics, and turbulent properties therein. The numerical simulation intended to reproduce an experimental setup, which exhibited a fast deflagration and eventually a flame-shock complex. The DNS observed the reaction as a flame-shock complex immediately upon flame initiation, although they maintained similar pressure transducer evolutions to the experimental profiles throughout the flow cycle. This difference emphasizes that we have not created an exact "one-to-one" numerical model of the TST facility, but rather a complementary numerical configuration based on an experimental facility which allows us to study the features of highly unsteady, extreme, propulsion-relevant regimes in detail. An exact numerical replica would require detailed chemical models and potentially a larger domain to include the turbulence generation section of the TST, neither of which are feasible with current HPC capabilities.

The flow regimes of the flame-shock complex studied are at simultaneously large length and velocity scales which push the boundary of what has been achieved by previous DNS studies. The high levels of M_f, Ka, and Re_λ indicate that this high-speed reacting flow is both highly compressible and highly turbulent, without the presence of any external turbulence driving.

The observed discrepancy between the results of fuel consumption rate and physical displacement based flame speed measurement techniques is present in both this configuration as well as several flame in the box studies involving several different types of reaction modes. The deviations seen can be significant and motivate further study to better determine the nature of the relationship between S_D and S_T in these and more extreme regimes where they differ appreciably.

Large turbulent flame speeds were measured using both methods and reached over 100 m/s for most of the simulation time. These flame speeds are approximately equal to the turbulent velocities seen in the simulations and indicate high turbulent intensities. PDF and enstrophy analysis show that a large amount of the turbulence generation occurs across the flame, independently of the turbulence in the inlet jets. This flame-generated turbulence, previously observed in the more idealized flame in the box simulations, was seen here in a realistic setting for the first time. The enstrophy budget shows a significant increase in vortex stretching and dilatation across the flame and into the products, while baroclinic torque is most significant in the flame brush itself.

In conclusion, this thesis successfully developed a numerical setup to study a realistic flow which is noteworthy in its ability to probe simultaneously high speed, strongly compressed, and highly turbulent regimes. This configuration can provide the foundation for further studies in realistic, propulsion-relevant, extreme regimes. This new canonical model shows that there are regions of flow at these regimes which could, individually, be represented by new LES models. These subdomains have been separated by axial variables and are effectively one-dimensional.

Going forward, realism can be improved on three fronts. First, the chemical model could be improved, or multi-step chemistry could be implemented. Second, domain boundaries could be modified. Not only is there room to improve the realism of the highly complex injection evolution, but the simple solid walls, currently modeled as adiabatic, could represent the actual isothermal walls. Finally, increasing numerical resolution would be beneficial. Although the flame is adequately resolved in case P08h, turbulent scales are currently resolved to, at best, one cell width. Furthermore, the bulk of the flow remains resolved by less than half a cell width, which is poor for a DNS.

REFERENCES

1. Chen, J., Petascale direct numerical simulation of turbulent combustion—fundamental insights towards predictive models. Proceedings of the Combustion Institute, 2011. **33**(1): p. 99-123.
2. Gicquel, L.Y.M., G. Staffelbach, and T. Poinsot, Large Eddy Simulations of gaseous flames in gas turbine combustion chambers. Progress in Energy and Combustion Science, 2012. **38**(6): p. 782-817.
3. Moureau, V., P. Domingo, and L. Vervisch, From Large-Eddy Simulation to Direct Numerical Simulation of a lean premixed swirl flame: Filtered laminar flame-PDF modeling. Combustion and Flame, 2011. **158**(7): p. 1340-1357.
4. Franzelli, B., E. Riber, L.Y.M. Gicquel, and T. Poinsot, Large Eddy Simulation of combustion instabilities in a lean partially premixed swirled flame. Combustion and Flame, 2012. **159**(2): p. 621-637.
5. Roux, S., G. Lartigue, T. Poinsot, U. Meier, and C. Bérat, Studies of mean and unsteady flow in a swirled combustor using experiments, acoustic analysis, and large eddy simulations. Combustion and Flame, 2005. **141**(1): p. 40-54.
6. Hawkes, E.R., O. Chatakonda, H. Kolla, A.R. Kerstein, and J.H. Chen, A petascale direct numerical simulation study of the modelling of flame wrinkling for large-eddy simulations in intense turbulence. Combustion and Flame, 2012. **159**(8): p. 2690-2703.
7. Dem, C., M. Stöhr, M. Christoph, A. Steinberg, and W. Meier, Experimental Study of Turbulence-Chemistry Interactions in Perfectly and Partially Premixed Confined Swirl Flames. Zeitschrift für Physikalische Chemie, 2015. **229**(4): p. 569.

8. Wang, P., N.A. Platova, J. Fröhlich, and U. Maas, Large Eddy Simulation of the PRECCINSTA burner. International Journal of Heat and Mass Transfer, 2014. **70**: p. 486-495.

9. Poludnenko, A.Y., T.A. Gardiner, and E.S. Oran, Spontaneous Transition of Turbulent Flames to Detonations in Unconfined Media. Physical Review Letters, 2011. **107**(5): p. 054501.

10. Hamlington, P.E., A.Y. Poludnenko, and E.S. Oran, Intermittency in premixed turbulent reacting flows. Physics of Fluids, 2012. **24**(7): p. 075111.

11. Hamlington, P.E., A.Y. Poludnenko, and E.S. Oran, Interactions between turbulence and flames in premixed reacting flows. Physics of Fluids, 2011. **23**(12): p. 125111.

12. Hamlington, P.E., R. Darragh, C.A. Briner, C.A.Z. Towery, B.D. Taylor, and A.Y. Poludnenko, Lagrangian analysis of high-speed turbulent premixed reacting flows: Thermochemical trajectories in hydrogen–air flames. Combustion and Flame, 2017. **186**: p. 193-207.

13. Kim, J., M. Bassenne, C.A.Z. Towery, P.E. Hamlington, A.Y. Poludnenko, and J. Urzay, Spatially localized multi-scale energy transfer in turbulent premixed combustion. Journal of Fluid Mechanics, 2018. **848**: p. 78-116.

14. Towery, C.A.Z., A.Y. Poludnenko, J. Urzay, J. O'Brien, M. Ihme, and P.E. Hamlington, Spectral kinetic energy transfer in turbulent premixed reacting flows. Physical Review E, 2016. **93**(5): p. 053115.

15. O'Brien, J., C.A.Z. Towery, P.E. Hamlington, M. Ihme, A.Y. Poludnenko, and J. Urzay, The cross-scale physical-space transfer of kinetic energy in turbulent premixed flames. Proceedings of the Combustion Institute, 2017. **36**(2): p. 1967-1975.

16. Poludnenko, A.Y. and E.S. Oran, The interaction of high-speed turbulence with flames: Turbulent flame speed. Combustion and Flame, 2011. **158**(2): p. 301-326.

17. Lee, J.H.S., The Detonation Phenomenon. 2008: Cambridge University Press.

18. Libby, P.A. and F.A. Williams, Turbulent Reacting flows. 1994: Academic Press.

19. Wolanski, P., Detonative propulsion. Proceedings of the Combustion Institute, 2013. **34**(1): p. 125 - 158.

20. Roy, G.D., F.S. M., A.A. Borisov, and D.W. Netzer, Pulse detonation propulsion: challenges, current status, and future perspective. Progress in Energy and Combustion Science, 2004. **30**(6): p. 545 - 672.

21. Chambers, J. and K. Ahmed, An Experimental Investigation of Fast Hydrogen-Air Flames and Detonations Using a Turbulence Generating Facility, in 55th AIAA Aerospace Sciences Meeting. 2017, American Institute of Aeronautics and Astronautics.

22. Chambers, J., K. Ahmed, and A.Y. Poludnenko, Exploration of Turbulence Driven Deflagration to Detonation of Fast Flames, in 26th ICDERS 2017: Boston, MA.

23. Zel'dovich, Y.B., V.B. Librovich, G.M. Makhviladze, and G.I. Sivashinskil, On the onset of detonation in a nonuniformly heated gas. Journal of Applied Mechanics and Technical Physics, 1970. **11**(2): p. 264-270.

24. Urtiew, P.A., A.K. Oppenheim, and S.O. Saunders, Experimental observations of the transition to detonation in an explosive gas. Proceedings of the Royal Society of London. Series A. Mathematical and Physical Sciences, 1966. **295**(1440): p. 13-28.

25. Kuznetsov, M., M. Liberman, and I. Matsukov, Experimental Study of the Preheat Zone Formation and Deflagration to Detonation Transition. Combustion Science and Technology, 2010. **182**(11-12): p. 1628-1644.

26. Oran, E.S. and V.N. Gamezo, Origins of the deflagration-to-detonation transition in gas-phase combustion. Combustion and Flame, 2007. **148**(1): p. 4-47.

27. Nettleton, M.A., Gaseous Detonations. 1987: Springer Netherlands. 256.

28. Khokhlov, A.M., Oran, E. S., and J. C. Wheeler, Deflagration-to-Detonation Transition in Thermonuclear Supernovae. The Astrophysical Journal, 1997. **478**(2): p. 678-688.

29. Gamezo, V.N., A.M. Khokhlov, and E.S. Oran, Deflagrations and Detonations in Thermonuclear Supernovae. Physical Review Letters, 2004. **92**(21): p. 211102.

30. Khokhlov, A.M., E.S. Oran, and J.C. Wheeler, A theory of deflagration-to-detonation transition in unconfined flames. Combustion and Flame, 1997. **108**(4): p. 503-517.

31. Poludnenko, A.Y., Pulsating instability and self-acceleration of fast turbulent flames. Physics of Fluids, 2015. **27**(1): p. 014106.

32. Chapman, D.L., VI. On the rate of explosion in gases. The London, Edinburgh, and Dublin Philosophical Magazine and Journal of Science, 1899. **47**(284): p. 90-104.

33. Jouguet, E., On the propagation of chemical reactions in gases. Journal des Mathematiques Pures et Appliquees, 1905-1906. **1-2**: p. 347-425, 5-85.

34. Gardiner, T.A. and J.M. Stone, An Unsplit Godunov Method for Ideal MHD via Constrained Transport in Three Dimensions. Journal of Computational Physics, 2008. **227**: p. 4123-4141.

35. Stone, J. M., Gardiner, T. A., Teuben, P., Hawley, J. F., and Simon, J. B., Athena: A New Code for Astrophysical MHD. The Astrophysical Journal Supplement Series, 2008. **178**(1): p. 137.

36. Poludnenko, A.Y. and E.S. Oran, The interaction of high-speed turbulence with flames: Global properties and internal flame structure. Combustion and Flame, 2010. **157**(5): p. 995-1011.

37. Gamezo, V.N., T. Ogawa, and E.S. Oran, Flame acceleration and DDT in channels with obstacles: Effect of obstacle spacing. Combustion and Flame, 2008. **155**(1): p. 302-315.

38. Kessler, D.A., V.N. Gamezo, and E.S. Oran, Simulations of flame acceleration and deflagration-to-detonation transitions in methane–air systems. Combustion and Flame, 2010. **157**(11): p. 2063-2077.

39. Chambers, J., K. Ahmed, A.Y. Poludnenko, and V.N. Gamezo, Spontaneous Runaway of Fast Turbulent Flames for Turbulence-Induced Deflagration-to-Detonation Transition 2019: Combustion and Flame. Under review.

40. Poludnenko, A.Y., J. Chambers, K. Ahmed, V.N. Gamezo, and B.D. Taylor, Universal Mechanism of the Unconfined Deflagration-to-Detonation Transition in Terrestrial Chemical Systems and Type Ia Supernovae 2019: Science. Under review.

41. Sosa, J., J. Chambers, K. Ahmed, A.Y. Poludnenko, V.N. Gamezo, Compressible Turbulent Flame Speeds of Highly-Turbulent Standing Flames. Proceedings of the Combustion Institute, 2018. In-press.

42. Towery, C., A.Y. Poludnenko, and P. Hamlington, Detonation initiation by compressible turbulence thermodynamic fluctuations: Combustion and Flame. Unpublished.

43. Borghi, R., On the Structure and Morphology of Turbulent Premixed Flames. 1985. p. 117-138.

44. Kolmogorov, A. N., V. Levin, J. C. R. Hunt, O. M. Phillips, and D. Williams, Dissipation of energy in the locally isotropic turbulence. Proceedings of the Royal Society of London. Series A: Mathematical and Physical Sciences, 1991. **434**(1890): p. 15-17.

45. Pope, S.B., Turbulent Flows. 2000: Cambridge University Press.

46. Im, H.G., P.G. Arias, S. Chaudhuri, and H.A. Uranakara, Direct Numerical Simulations of Statistically Stationary Turbulent Premixed Flames. Combustion Science and Technology, 2016. **188**(8): p. 1182-1198.

47. O'Neill, L., A.Y. Poludnenko, K. Ahmed, J. Chambers, and V.N. Gamezo. How Fast is the Flame: Displacement vs. Burning Speeds of Fast, Highly Compressible Turbulent Premixed Flames. in American Physical Society Division of Fluid Dynamics. 2018. Atlanta, GA.

48. Kazbekov, A., K. Kumashiro, and A. Steinberg, Enstrophy transport in swirl combustion, in Journal of Fluid Mechanics. 2018.

49. Gao, Y. and T. Lu, Reduced HyChem Models for Jet Fuel Combustion. 2017.

50. Fureby, C., On the Supersonic Flame Structure in the HyShot II Scramjet Combustor, in 26th ICDERS. 2017: Boston, MA, USA.

51. Kozak, Y., et al., Novel Lagrangian-Particle Tracking Method for Highly Compressible, Turbulent, Reacting Flows, in AIAA Scitech 2019 Forum. 2019, American Institute of Aeronautics and Astronautics.

52. Kozak, Y., et al., WENO interpolation for Lagrangian-Particle Tracking Analysis of Highly Compressible Reactive Flows 2019: Journal of Computational Physics. Unpublished.

53. Dammati, S.S., Y. Kozak, L. O'Neill, P.E. Hamlington, and A.Y. Poludnenko. Lagrangian Analysis of Thermo-Chemical Trajectories in High Speed, Turbulent, Premixed n-Dodecane-Air Flames. in American Physical Society Division of Fluid Dynamics. 2018. Atlanta, GA.

APPENDIX A

ALTERNATIVE SETUP: SWIRL COMBUSTOR

Prior to implementing and studying the TST configuration, work was done with a DLR-type PRECCINSTA burner swirl combustor. Simulation was performed using the same Athena-RFX code and single-step Arrhenius kinetics with a methane-air mixture. As discussed in Chapter I, this DNS implemented a simplified chemical model on a realistic swirl combustor setup. While the configuration's simulation capabilities were limited to moderate, atmospheric conditions, the scale of the DNS was considerable. The domain size spanned 4.5 cm in the transverse directions and over 12 cm in the axial direction resulting in a cell size of just over 20 μm.

Numerically replicating realistic injection conditions of the swirl inflow is particularly challenging and preliminary efforts were made to collaborate with Pierre Bénard and Vincent Moreau at CORIA for injection data to implement more realistic injection flow dynamics. Their LES simulation domains include the plenum and swirler regions in addition to the combustion chamber itself. The nonreacting gas in the swirler can be modeled with high accuracy using LES and thus could provide suitable injection plane conditions. Further work with this configuration should use such data for the injection boundary conditions. Completed analysis focused on general flow dynamics and, specifically, enstrophy budget analysis which is detailed in Figure 26. The left column shows enstrophy budget components with $i = 1$ and the right side with $i = 3$ components.

Vortex stretching and viscous dissipation can be present in both reacting and nonreacting flow, while dilatation and baroclinic torque are contributed mainly by the flame [48]. In this configuration, vortex stretching is the main contributor to the enstrophy budget while the effects of viscous dissipation are relatively minimal. Both baroclinic torque and dilatation are reasonably

significant, which implies that the flame plays an active role in the turbulence dynamics of this swirl combustor.

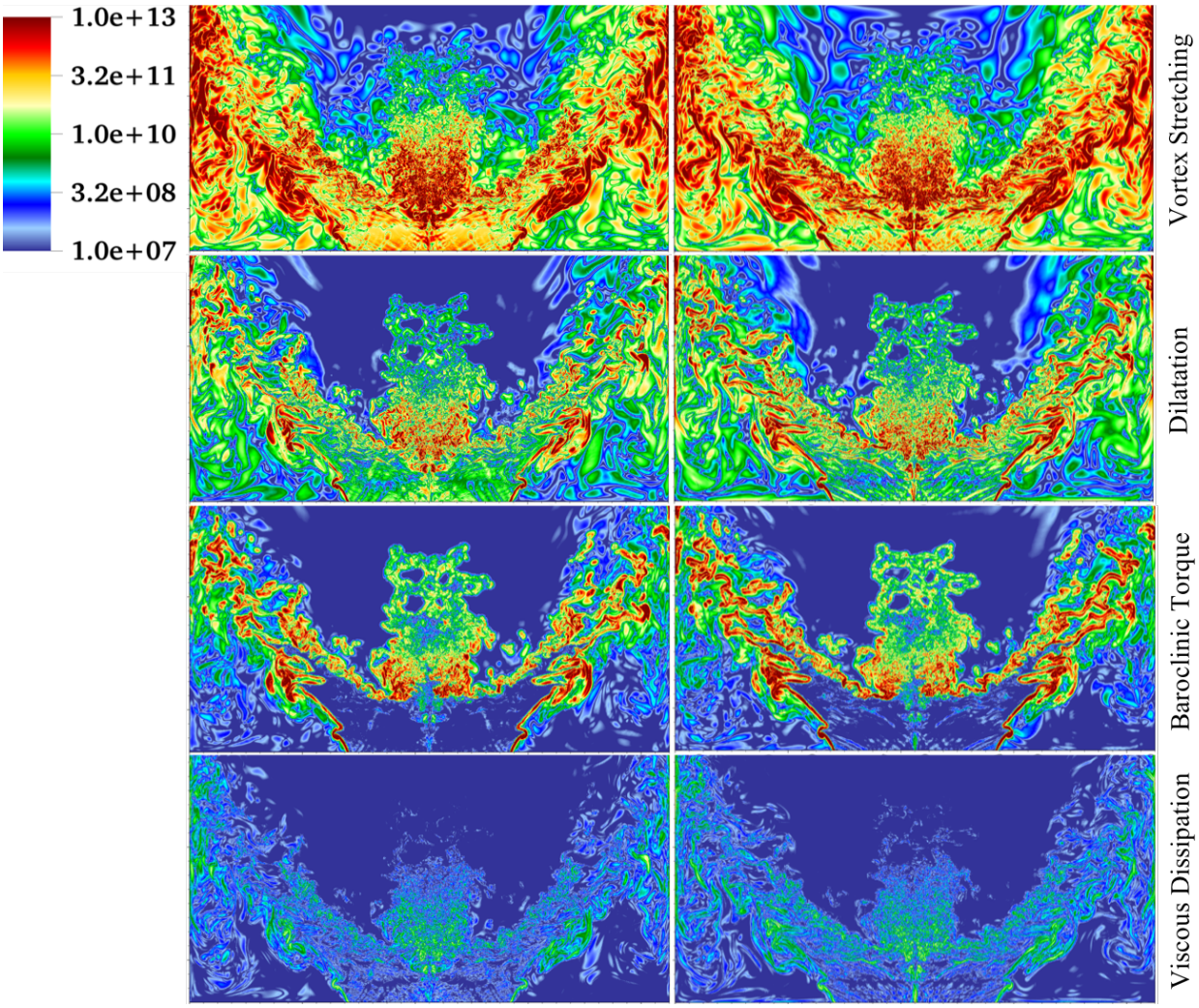

Figure 26 Enstrophy budget analysis for the DLR-type PRECCINSTA burner swirl combustor with the axial direction cropped at ~2 cm.

APPENDIX B

ALTERNATIVE CHEMISTRY: MULTI-STEP

While the primary topic of this thesis is of extreme reacting flows in realistic physical settings attainable only by conceding a significantly simplified reaction model, a series of DNS using complex chemical models for n-dodecane at various high Karlovitz numbers in Kolmogorov-type driven turbulence was performed. These flame in the box DNS use the PREMIX code of the CHEMKIN-II package to supply laminar flame properties, with the fuel cracking and oxidization mechanisms of n-dodecane modeled using a reduced kinetics model based on the HyChem concept [49].

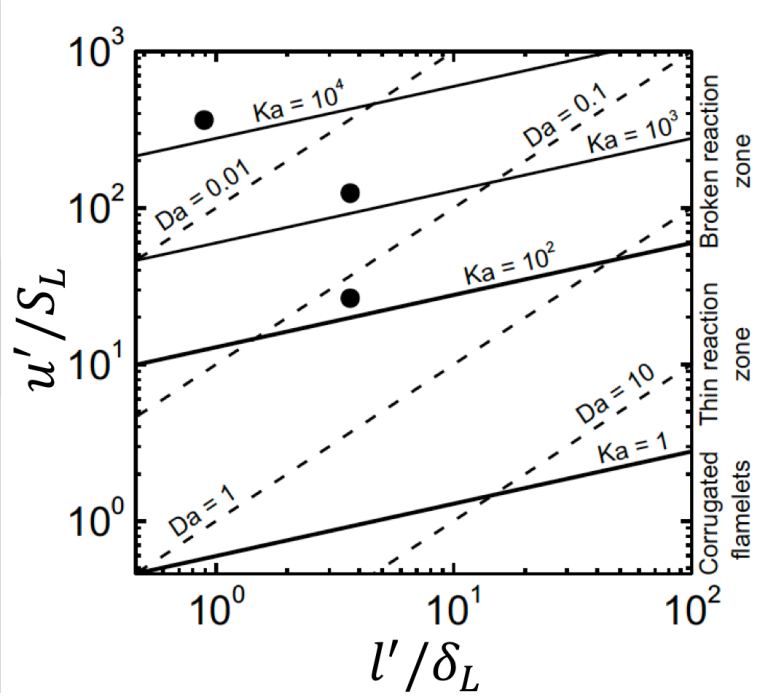

Figure 27 Borghi diagram for realistic flame in the box n-dodecane DNS.

The goal of this study is to understand the flame-turbulence interactions in extreme turbulent combustion regime of distributed reaction zones, where small-scale turbulent flow structures begin to penetrate into the reaction zone and transport heat from the reaction zone to the

pre-heat zone which can ultimately lead to the breakdown of chemistry and flame extinction. These extremely high turbulent regimes are of particular interest to scramjet applications. LES carried out by Fureby have observed flames in scramjet combustors subject to turbulent Mach numbers up to 0.75 [50]. The Borghi regime diagram for the various Karlovitz number cases, Ka = 100, Ka = 1,000, and Ka = 10,000, is shown in Figure 27. While the normalized velocity scales achieved are certainly appreciable, the normalized length scales are small, as is common with flame in the box DNS.

The Lagrangian particle tracking analysis allows the direct calculation of residence times and path lengths of massless particles (fluid parcels) and is the first such study to be performed in these extreme regimes. Symplectic integrators and a WENO-based integration approach proposed by Kozak et al. [51, 52] have been incorporated into Athena-RFX to achieve accurate particle tracking over long integration times and across sharp discontinuities, which are inherent to these regimes.

The primary analysis thus far has focused on the n-dodecane, $Ka = 10{,}000$ case. For these simulations, the three-dimensional $1{:}8$ domain is initially filled with n-dodecane fuel with $\phi = 0.7$ at 700 K and 30 atm. Homogenous isotropic turbulence is stochastically driven at the large scales, and the flow field is allowed to evolve for two eddy turn-over times to allow turbulence to reach an equilibrium. After this, a statistically planar flame is initiated in the transverse plane at the midsection of the axial domain and is allowed to develop for one additional eddy turn-over time, at which point the flame speed reaches a statistically stationary state. The particles are then injected onto an isothermal surface of 800 K and tracked for the final three eddy turn-over times.

A highly complex thermo-chemical phase space evolution was observed which indicates non-monotonicity and enhanced molecular transport in these regimes. While most particles remained in the pre-heat and pyrolysis zones after the full 6 eddy turn-over time simulation was completed, a small subset of particles which burned and reached the product zone, were analyzed. These so-called “fast burner” particles experience very short residence times – the time a particle spends at a temperature interval, e.g. 800-1000 K which is indicative of the flame pre-heat zone. The flame crossing residence times (800-2100 K) for the fast burners is shorter even than the chemical pyrolysis time scale. This raises questions as to the validity of the HyChem premise, which expects pyrolysis to precede oxidation, whereas here, pyrolysis was observed to continue past 1500 K, the upper limit of the maximum heat release rate zone. [53]